

Development of idealized practices for photoacoustic spectroscopy

by

©Stephen Campbell

A thesis submitted to the School of Graduate Studies in partial fulfillment of the
requirements for the degree of

Master of Science

Department of Physics and Physical Oceanography

Memorial University of Newfoundland

August 2017

St. John's

Newfoundland

Abstract

Fourier Transform Infrared (FTIR) spectroscopy is an experimental technique used to characterize materials based on molecular vibrations. Infrared light is absorbed by the sample which excites molecular vibrations. Based on the specific vibrations it is possible to determine the composition and information related to structural ordering. Photoacoustic FTIR spectroscopy (FTIR-PAS) combines FTIR with acoustic detection of the infrared absorption. My thesis work focused on investigating FTIR-PAS scan parameters to further develop FTIR-PAS as a quantitative materials characterization method. Based on those results I presented a set of best practices for data collection. I then investigated size related effects on the PAS measurement by applying those best practice parameters to silica spheres. Overall signal intensity increased with decreasing particle size, which has been previously reported. No peak position, shape or relative intensities changes were found. These insights were used to evaluate previously collected calcite data and support previous conclusions that observed effects were related to sample and detection method differences.

Acknowledgements

My deepest thanks and appreciation to my supervisor, Dr. Kristin M. Poduska. For initially inviting me into her research group and for her constant guidance, compassion and patience throughout this project thereafter, I am forever grateful. I wish to thank Dr. Kirk Michaelian for his help in furthering my education on photoacoustic spectroscopy, and for his speed and patience in answering my many questions.

I would like to thank the Poduska Group research members past and present, for laying the ground work for this research and for their help and support while I brought this work to its current state.

I would like to thank Regan and the rest of my family for their support during this venture and throughout my life. This accomplishment is as much theirs as it is mine.

Finally, I thank the National Sciences and Engineering Research Council, the Department of Physics and Physical Oceanography and the School of Graduate Studies for their financial support.

Table of Contents

Abstract	ii
Acknowledgments	iii
Table of Contents	vi
List of Tables	vii
List of Figures	xii
List of Abbreviations and Symbols	xii
1 Introduction	1
1.1 The importance of crystal structures	1
1.2 Vibrational modes in solids	2
1.3 Infrared Spectroscopy	4
1.3.1 Optical detection (FTIR-Op)	6
1.3.2 Photoacoustic detection (FTIR-PAS)	7
1.3.3 Comparing optical and photoacoustic detection of IR absorption	8
1.4 Thesis overview	9
2 Developing best practices for PAS measurements	11

2.1	Sample preparation	13
2.2	Inside the spectrometer	13
2.2.1	Infrared beam generation	14
2.2.2	Acquisition method	16
2.2.3	Mirror speed	16
2.2.4	Co-additions	22
2.2.5	Detection of IR absorption by the sample	23
2.2.5.1	FTIR-Op	23
2.2.5.2	FTIR-PAS	25
2.3	Data processing	26
2.3.1	Preparing for the Fast Fourier Transform	26
2.3.2	Phase correction	28
2.3.3	Signal Correction	35
2.4	Best practices	35
3	Using best practices	40
3.1	Experimental details	41
3.1.1	Silica spheres	41
3.1.2	Photoacoustic measurements of silica	41
3.1.3	Transmission measurements of silica	43
3.2	Motivation	43
3.3	Results and Discussion	45
3.4	Connections with past FTIR-Op investigations	46
3.5	Conclusions	50
4	Conclusions	52
4.1	Summary	52

4.2 Broader context	54
Bibliography	55

List of Tables

1.1	The characteristic normal modes of α -SiO ₂ . Values are taken from Al-Oweini <i>et al.</i> [1]. Values based on infrared spectroscopic measurements of compounds synthesized using two common precursors.	3
1.2	A summary of possible observed spectral changes and the sample differences attributed as the cause.	6

List of Figures

1.1	Representation of the silica tetrahedron (SiO_4) indicating bending and stretching vibrations. In the fully crystalline state, the tetrahedrons are repeated such that symmetry is maintained over both short-range and long-range order. In the amorphous state, long-range order is lost due to lattice defects. The general types of local vibrational modes (stretching and bending) are indicated with arrows. This image is a modified version of the original, used as part of the CC-PD.	3
1.2	Characteristic Mid-IR spectrum of amorphous silicon dioxide (silica). The vibrational modes at 1100 cm^{-1} and 1200 cm^{-1} correspond to the Si-O stretching modes. Si stretching and Si-O-Si bending are observed at 850 cm^{-1} and 460 cm^{-1} respectively.	5
1.3	Representative FTIR spectrum of 250 nm silica particles. Data were collected using the FTIR-Op (top) and FTIR-PAS (bottom) detection schemes. Positions of the vibrational modes remain unchanged, but there are changes to peak shapes and intensities.	9

2.1	A schematic picture of the FTIR spectrometer highlighting the use of a Michelson interferometer. The infrared source (A) generates the initial beam. The beam splitter (B) divides the initial IR beam into two beams with half of the original source intensity. The stationary mirror (C) and the moving mirror (D) are used to create a path difference for the two beams, resulting in interference. After recombining at the beam splitter the IR beam is incident on the sample (E) with the final interferogram being recorded at the detector (F, FTIR-Op) or in the PAS cell (E, FTIR-PAS).	15
2.2	Spectra of 100 nm silica particles with different acquisition directions. The spectral data were Fourier Transformed from the backward interferogram (red), forward interferogram (black) and the average of both the forward and backward spectral data (blue). All three acquisition methods produce nearly identical data. Minor deviations in signal intensity are observed around many of the peaks, the largest being the feature at 600 cm^{-1} which is a difference of less than 1% of the intensity.	17
2.3	PAS spectrum of silica with mirror speeds of 1.6 kHz (black), 2.5 kHz (red) and 5.0 kHz (blue). The slower mirror speed data are in good agreement in terms of peak positions, relative intensities and widths. the 5.0 kHz data shows obvious changes in relative peak heights at 2900 cm^{-1} , 1200 cm^{-1} and 500 cm^{-1} possibly attributed to resonance effects.	18

2.4	(a) Magnitude spectra of 100 nm silica measured with mirror speeds of 1.6 kHz (black), 2.5 kHz (red) and 5.0 kHz (blue). There is a significant change in the peak structures above 1800 cm^{-1} in the 5.0 kHz data. Below this peaks maintain shape and position, with higher intensities at slower speeds. (b) The mirror speed is adjusted (5 kHz, 2.5 kHz and 1.6 kHz) for 250 nm silica particles, plotted as a function of modulation frequency. The resonance peak around 800Hz is a feature of the photoacoustic cell. The resonance spike causes the 5 kHz data to diverge significantly from the others. Plots created by collaborator K. Michaelian (NRC CanmetENERGY, Edmonton) using my data.	20
2.5	Magnitude plots of the carbon black reference sample measured with mirror speeds of 1.6 kHz (black), 2.5 kHz (red) and 5.0 kHz (blue). As with the silica sample shown in Figure 2.4a there is a change to peak shapes above 1800 cm^{-1} using a mirror speed of 5.0 kHz.	21
2.6	FTIR-PAS spectrum of 100 nm silica particles using 4 scans (black) and 128 scans (blue). The increase in co-additions results in a higher signal-to-noise ratio. There is an overall loss of intensity with increasing co-additions.	23
2.7	Center region (1000 of 14732 points) of a double-sided interferogram recorded from a FTIR-PAS experiment using 250 nm silica particles. The interference of the IR beams causes regions of high and low intensity as the mirror displacement changes.	24

2.8	A schematic picture of the photoacoustic cell. The interfered IR beam enters the cell, and is incident on the sample. This causes thermal expansion/contraction in the sample, giving rise to a pressure wave in the carrier gas. The pressure wave is detected by the cantilever and saved as an interferogram.	25
2.9	Center region (1000 out of 14732 points) of an unprocessed interferogram (intensity <i>vs.</i> mirror displacement). The red line is mean of the data set. The interferogram is normalized <i>via</i> mean subtraction from each datum.	27
2.10	The normalized interferogram. Vertical lines mark the next power of 2 and the number of points which marks a zerofilling factor of 2.	28
2.11	The centerburst data subset that will be used to prepare the phase correction data. A basic triangular window function is overlaid. The two will be multiplied together during apodization.	29
2.12	A computer generated signal comprised of two main frequencies (black) and the output of the FFT algorithm. Leakage aberrations are indicated. The same generated signal is multiplied by a Blackman-Harris 3-Term window function (blue) before applying the FFT algorithm. By windowing, nearly all of the leakage aberrations have been removed. Figure is adapted from Ref. [2].	31
2.13	Changing the window function used in the FFT procedure results in negligible changes to the output spectrum. Three different windowing functions were used: Triangular (blue), Blackman-Harris 3-Term (black) and Norton-Bier, Medium (red).	32
2.14	The apodized, zerofilled centerburst data is rotated such that the data prior to the centerburst are place at the end.	33

2.15	The Real and Imaginary component results of the FFT algorithm on the manipulated centerburst data. The phase angle is calculated from these arrays according to Equation 2.2	34
2.16	Magnitude spectrum produced as the final result of the phase corrected, Fourier transformed interferogram. Using the phase angle calculated by Equation 2.2, this result is produced from Equation 2.3.	34
2.17	FTIR-PAS spectrum of 100 nm silica spheres using the Mertz (black) and modulus (green) phase correction methods. A wavelength dependent intensity difference is observed at lower wavenumbers. Peak widths remain unchanged between the correction methods, while peak positions shift approximately 2 cm^{-1}	36
2.18	FTIR-PAS spectrum of the sample and reference. Background correction is accomplished by dividing the sample by the reference.	37
3.1	FTIR-PAS spectra of varying sized silica spheres. There is a clear increase in spectral intensity with decreasing particle size. This is attributed to the increase in surface area producing the thermal wave. Particle size appears to have no effect on peak positions, widths or relative intensities.	45

List of Abbreviations and Symbols

DFT	Density functional theory
FFT	Fast Fourier Transform
FTIR	Fourier Transform Infrared Spectroscopy
FTIR-Op	Optical FTIR
FTIR-PAS	Photoacoustic FTIR
IR	Infrared
PAS	Photoacoustic Spectroscopy
Mid-IR	Mid-range infrared
XRD	X-Ray diffraction
ZPD	Zero path difference

Chapter 1

Introduction

1.1 The importance of crystal structures

Materials scientists concern themselves with the properties of materials and the underlying arrangement of the atoms that gives rise to those properties. Consider graphite and diamond; both materials are built from arrangements of carbon atoms. Each of these materials is crystalline; a small group of atoms is repeated at every point on a lattice, which is itself a repeating pattern of points in space. This endlessly repeating collection of atoms makes up the macroscopic body. One may describe the entire system using smallest repeating piece of the arrangement, the unit cell [3]. Strictly speaking, this perfectly repeating collection of atoms is not exactly the case, as defects may be present such as elemental substitutions or distortions in the lattice.

Returning back to the crystalline carbon substances, graphite and diamond, it is plain to see that these are two very different materials macroscopically. Viewed in the visible regime, diamond appears transparent while graphite is black. Diamond is the hardest natural material known, while graphite is quite soft. The two also differ in their electrical properties; diamond is an insulator while graphite is electrically

conductive. All of these differences are determined by the different arrangement of the carbon atoms.

1.2 Vibrational modes in solids

Vibrational modes of solids can be used to probe the structure of a sample [4]. The long-range ordering of a sample makes it crystalline, where only having short-range order gives it the classification of amorphous. Polymorphs of silicon dioxide (SiO_2) are useful examples to represent these two levels of crystallinity. Silicon dioxide is arranged atomically as a collection of interconnected tetrahedra composed of one silicon atom and four oxygen atoms (See Figure 1.1). When these tetrahedrons are repeated uniformly, the system is said to be the crystalline solid, c- SiO_2 , known also as quartz. When the long-range ordering is destroyed, such as by changes in bond angles between the atoms, the solid is said to be amorphous. The amorphous form of silicon dioxide, a- SiO_2 , is commonly known as silica. Even though both polymorphs have the same chemical composition, the vibrational modes will differ because of the differences in the atomic arrangements.

Vibrational modes can be subdivided into two categories: higher energy local modes (above $\sim 500 \text{ cm}^{-1}$) and lower energy lattice modes (below $\sim 500 \text{ cm}^{-1}$). Figure 1.1 shows two types of local modes related to the oscillations within a single SiO_4 moiety, stretching vibrations and bending vibrations. These vibrations can be conceptualized by considering the atoms and molecular bonds as a mass-spring system in which the atoms oscillate in various ways in relation to each other. The energies of vibrational modes of interest in a- SiO_2 are reported in Table 1.1. The silica bands have been previously reported by many others [1,5–12]. Other modes may be present, related to surface groups such as silanol (SiOH) or adsorbed water vibrations.

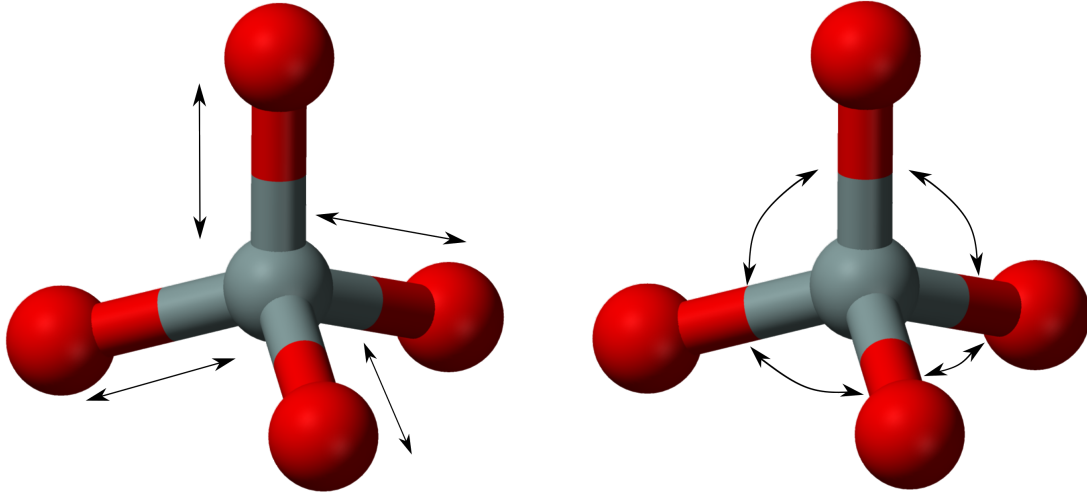


Figure 1.1: Representation of the silica tetrahedron (SiO_4) indicating bending and stretching vibrations. In the fully crystalline state, the tetrahedrons are repeated such that symmetry is maintained over both short-range and long-range order. In the amorphous state, long-range order is lost due to lattice defects. The general types of local vibrational modes (stretching and bending) are indicated with arrows. This image is a modified version of the original, used as part of the CC-PD.

Table 1.1: The characteristic normal modes of a- SiO_2 . Values are taken from Al-Oweini *et al.* [1]. Values based on infrared spectroscopic measurements of compounds synthesized using two common precursors.

Feature	Wavenumber (cm^{-1})	Description
ν_{as} Si-O-Si	1200	Asymmetric stretching
ν_{as} Si-O-Si	1089-1095	Asymmetric stretching
ν_b Si-O	961-965	In-plane stretching
ν_s Si-O	799-800	Symmetric stretching
ν Si-O	558-560	Stretching vibration
δ O-Si-O	467-469	Lattice deformation

Each specific mode has a characteristic resonance frequency associated with it and will absorb energy that corresponds to that frequency. Local modes are generated within a specific moiety, such as the oscillations of the oxygen atoms against the silicon atom within a single SiO_4 tetrahedron. The lower energy lattice modes are the excitations related to the movement of a collection of atoms in concert such as the twisting of many tetrahedra.

1.3 Infrared Spectroscopy

The energies of infrared light and the vibrational modes of a solid are on the same order of magnitude. Thus, it is possible to excite these vibrational modes by irradiating the system with infrared light, causing the resonance oscillations. This is a common tool used for chemical identification, as each compound will have a unique infrared (IR) spectrum. The fundamental vibrational regime is the Mid-range infrared (Mid-IR) covering 4000 cm^{-1} - 400 cm^{-1} (about $2.5\text{ }\mu\text{m}$ - $25\text{ }\mu\text{m}$). This type of spectrum, which is used in many fields and not specific to one IR detection method, is often referred to as a fingerprint spectrum [13–22]. While vibrational spectroscopy data cannot be used to extract crystal structure, it can be used to rapidly identify interesting changes among a collection of samples; highlighting those of interest which could then be examined further with other techniques.

A characteristic fingerprint spectrum of silica is shown in Figure 1.2. Absorption bands related to water (2900 cm^{-1} - 4000 cm^{-1} and 1400 cm^{-1} - 1800 cm^{-1}) and CO_2 (2400 cm^{-1} , 1150 cm^{-1} and 665 cm^{-1}) are artifacts of the experimental procedure and can be ignored. Sample related absorption bands correspond to the Si-O stretching (1100 cm^{-1} and 1200 cm^{-1}), Si stretching (850 cm^{-1}) and Si-O-Si bending (460 cm^{-1}). By examining these types of spectra for changes it is possible to

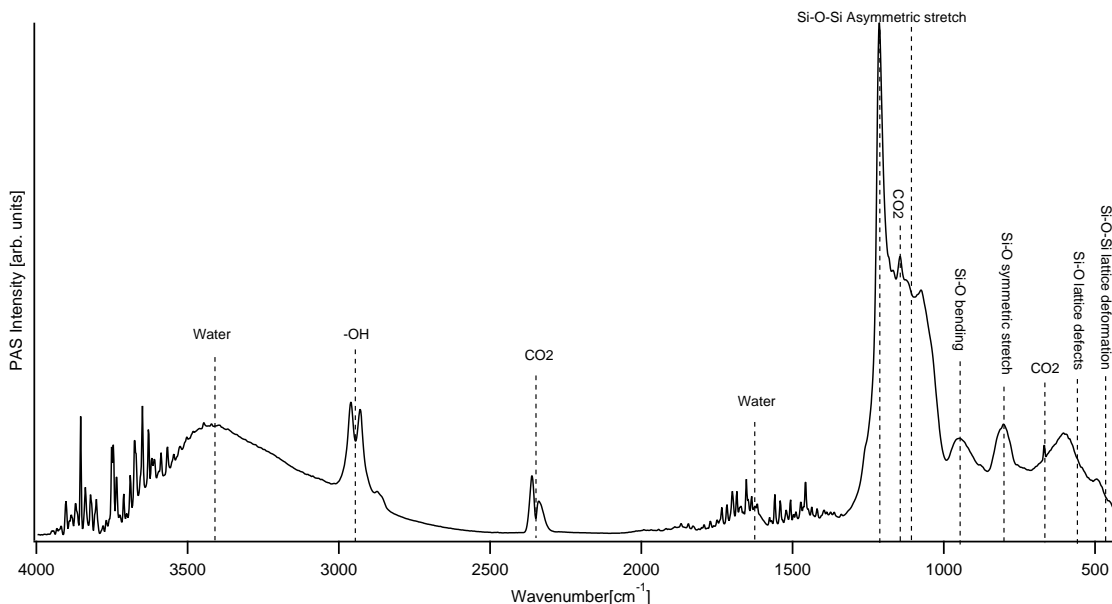


Figure 1.2: Characteristic Mid-IR spectrum of amorphous silicon dioxide (silica). The vibrational modes at 1100 cm^{-1} and 1200 cm^{-1} correspond to the Si-O stretching modes. Si stretching and Si-O-Si bending are observed at 850 cm^{-1} and 460 cm^{-1} respectively.

infer differences related to the sample, as the vibrational modes are directly related to structure [23,24]. Table 1.2 summarizes common spectral changes and the underlying sample related cause.

The most commonly used method of infrared spectroscopy is Fourier Transform Infrared (FTIR) spectroscopy. FTIR was developed as a means to reduce data acquisition times of the original dispersive IR spectrometers. The IR source light interferes with itself *via* an interferometer. The light is modulated at different frequencies as a function of wavenumber, ν . The beam then interacts with the sample which will absorb some of the light. This allows for simultaneous acquisition over a wider spectral region.

Changes in structural ordering such as degree of crystallinity or molecular arrangements are observed by examining the FTIR spectrum for differences in peak positions, shapes, widths as well as absolute and relative intensities [23–26]. Peak po-

Table 1.2: A summary of possible observed spectral changes and the sample differences attributed as the cause.

Spectral feature	Sample related change
Peak position	Structural change
Peak shape	Detection geometry, scattering
Peak width	Thermal effects, atomic ordering, detection geometry
Absolute peak intensity	Sample amount
Relative peak intensity	Crystallinity change

sitions correspond to the energy of the vibrational modes allowed within the sample. The modes are dependent on the atoms involved and their configuration in both the local environment (i.e. unit cell) and over longer range ordering related to the overall sample crystallinity. These FTIR peak positions can be calculated *via* using density functional theory (DFT) [23,24]. Changes in peak widths have been linked to atomic ordering and optical absorption effects [26]. Relative peak intensities have also been shown to be affected by atomic ordering in calcium carbonate materials with varying degrees of crystallinity [25].

1.3.1 Optical detection (FTIR-Op)

Following the IR beam absorption by the sample, the remaining beam is incident on the detector and recorded as an interferogram (Intensity vs. mirror displacement, $I(x)$). This interferogram is Fourier transformed according to the equation:

$$T(\nu) = \frac{2}{\pi} \int_{-\infty}^{\infty} dx I(x) e^{-i\nu x} \quad (1.1)$$

to produce the transmittance spectrum, $T(\nu)$ (Intensity vs wavenumber). Also commonly reported is the absorbance spectrum, $A(\nu)$, which is simply $A(\nu) = -\log[T(\nu)]$. In this thesis, this method of detection is referred to as Optical FTIR (FTIR-Op) and is the standard method of detection for FTIR spectroscopy in the literature.

Optical FTIR measurements involve mixing the sample into a high quality optical dilutant to avoid saturation in the resultant spectrum. Potassium bromide is commonly used for its IR transparency. The dilute mixture is pressed into a pellet which is placed in the IR beam path to obtain the absorbance/transmittance spectrum. While this technique is fast and generally non-destructive, the sample used is not recoverable. Furthermore, samples that cannot be properly dispersed throughout the dilutant result in strong absorption effects and ultimately fail to produce usable data.

1.3.2 Photoacoustic detection (FTIR-PAS)

Alexander Graham Bell first observed the photoacoustic effect in 1880 [27]. He and his colleagues found that when a modulated beam of light was incident on numerous substances, they produced audible sound. The photoacoustic effect was used primarily for gas analysis until the 1970s when the phenomena was applied to solids [28,29]. Theoretical studies by Rosencwaig and Gersho [30] as well as McDonald and Wetzel [31] postulated the idea that the detected photoacoustic signal is generated due to the periodic heat flow from the sample into the surrounding carrier gas. A summary of current techniques and many recent developments related to various samples was published by K. Michaelian [16]. The author discusses the evolution of the technique from the single-wavelength photoacoustic measurements of gases in the 1970s to the rapid scanning FTIR measurements of the 1980s and beyond. A comprehensive description of various experimental methods and data analysis techniques is given.

FTIR-PAS relies on the application of the photoacoustic effect. When modulated infrared light is incident on a sample, some of the energy is absorbed. This results in heating within the sample and producing thermal waves within the bulk. The thermal waves cause a cyclic expansion and contraction. The sample is in contact with the

atmosphere inside the detector, known as the carrier gas. The cyclic expansion of the sample produces a pressure wave in the carrier gas which is detected acoustically *via* a microphone or cantilever. This signal is recorded as an interferogram. The Fourier Transform of this interferogram is the photoacoustic signal of the sample.

What is evident is that FTIR-PAS, like FTIR-Op, is an incredibly useful technique for fingerprint identification of a sample. In an effort to strengthen FTIR-PAS as a screening tool, it was necessary to develop a understanding of the method greater than the typical use. The goal of this thesis was to identify instrumentation artifacts within the FTIR-PAS spectrum of a known material by making controlled changes to various data collection and processing parameters. Ultimately, the identification of spectral changes related only to structural differences in the sample is what will bring FTIR-PAS into the realm of screening techniques for material science.

1.3.3 Comparing optical and photoacoustic detection of IR absorption

It is important to note that both FTIR-Op and FTIR-PAS make use of the same IR source and differ only in the detection method. Data collected for the same sample under both conditions will produce two spectra with similarities in peak positions and peak intensities, but drastically different peak shapes. This can be plainly seen in Figure 1.3. The spectrum is annotated to indicate which vibrational mode is attributed to each peak. Some of the peaks present are related to other molecules present, such as water or carbon dioxide.

FTIR-Op is straight-forward; the light absorbed by the sample is inferred from the detector signal. An optically detected FTIR peak is the result of the sample absorbing the IR light at the specific energy corresponding to the vibrational mode. This is observed as the absence of the energy from the final beam at the detector.

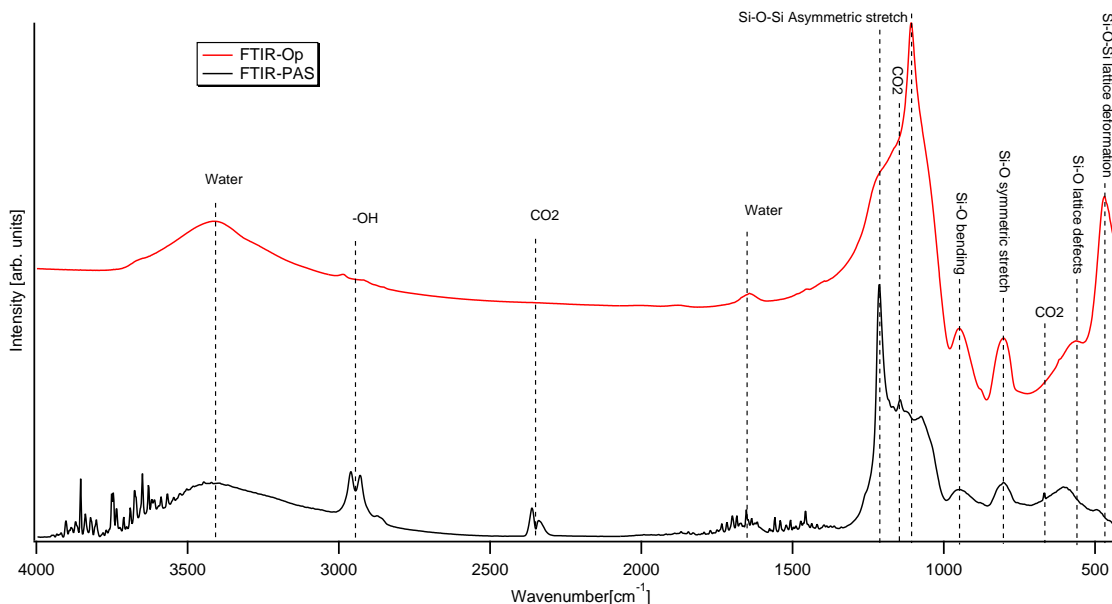


Figure 1.3: Representative FTIR spectrum of 250 nm silica particles. Data were collected using the FTIR-Op (top) and FTIR-PAS (bottom) detection schemes. Positions of the vibrational modes remain unchanged, but there are changes to peak shapes and intensities.

The detection method is fundamentally different in FTIR-PAS but the IR source remains the same. The thermal nature of the process is expected to cause peak broadening as the heating of the sample affects the vibrational modes. Given that every peak will have an inherent width, and that those widths may cause features to overlap, what presents as a single spectral feature can, in fact, be a combination of multiple allowed vibrations. The broadening does not appear to effect all peaks uniformly. This leads to significant changes in peak shapes for otherwise clean features in FTIR-Op.

1.4 Thesis overview

In this thesis, I focus on developing FTIR-PAS as a materials screening technique, in the hopes that it could be better used to differentiate samples based on observed

differences in the vibrational modes. To accomplish this, this work focuses on two main questions related to FTIR-PAS:

1. What spectral differences are artifacts caused by instrumentation and data collection procedures?
2. Do particle size differences in the sub-micron regime change FTIR-PAS spectra?

Chapter 2 takes an in-depth look at the step-by-step procedure of a FTIR experiment. Given the overlap between both FTIR-Op and FTIR-PAS, both methods are included in the discussion. The ideas of sample selection and preparation are examined, as well as various parameters involved in data collection and processing related to the spectrometer and the Fourier Transformation of the data. Chapter 3 showcases the application of the best practices from Chapter 2 by examining the effect of controlled size silica particles on the FTIR-PAS spectrum. A discussion regarding previous data in the context of the best practices is also included. Chapter 4 summarizes the main points of my thesis work.

Chapter 2

Developing best practices for PAS measurements

This investigation sought to strengthen FTIR-PAS as a screening tool for materials characterization. To accomplish this I needed to develop an understanding of FTIR-PAS beyond the standard use as a fingerprint identification technique. Using a Bruker Vertex 70v FTIR spectrometer with a Gasera PA-301 photoacoustic cell, I took measurements of AngströmSphere monodisperse silica particles. Silica produces a relatively simple IR spectrum and the availability of manufactured particles with a well defined size and shape made this an ideal sample for this investigation.

Each measurement was conducted on a range of particle sizes whilst varying a single experimental parameter. The removal of artifacts related to instrumentation, data collection and data processing procedures would be ideal to develop FTIR-PAS as a sample screening technique. By eliminating the spectral artifacts, any remaining differences should be attributed to the sample.

The experimental procedure I used to collect FTIR data can be broken into three major components: sample preparation, spectrometer operation and data processing.

A general description of the measurement procedure is outlined below. These points are expanded upon throughout the rest of the chapter and are accompanied by a discussion of the effects of each variable. Sample preparation is discussed in Section 2.1. The operation of the spectrometer is outlined in Section 2.2. Finally, a step-by-step procedure of the data processing is laid out in Section 2.3. All measurements and analyses were done by me at Memorial University of Newfoundland, St. John's campus. Our collaborator, Dr. Kirk Michaelian (NRC CanMET Energy, Alberta Canada), assisted with some of the data analysis and interpretation.

1. Sample preparation

- KBr (KCl) pellet (FTIR-Op)
- Sample cup packing (FTIR-PAS)

2. Software scan parameters

- Mirror speed
- Acquisition method
- Co-additions
- Phase correction
- Windowing function

3. Execute Measurement

- IR beam interference *via* Michelson interferometer
- IR beam interacts with sample
- Interferogram collected *via* detector

4. Data processing

- Fourier Transform as set in parameter selection
- Vacuum background (FTIR-Op) or reference sample (FTIR-PAS) scan
- Background correction *via* ratioing

2.1 Sample preparation

Depending on the type of sample, it may be necessary to change the detection method from the more common FTIR-Op to the less common FTIR-PAS. This choice also effects the sample preparation.

FTIR-Op requires mixing the sample with an IR inactive optical grade dilutant, such as potassium bromide, before pressing the sample into a pellet roughly 3 mm in diameter and 0.25 mm thick. The ratio of sample to dilutant is approximately 1:100. The amount of sample used in this mixture is crucial; too much will result in too much absorption while too little can lead to low signal-to-noise. The dispersion of the sample in the mixture can also affect the final spectrum [26]. Samples that cannot be dispersed in KBr (oils, tars, etc.) are not suited for FTIR-Op. FTIR-PAS samples do not need to be diluted, nor pressed into a pellet. The sample is simply placed in a sample cup with a 10 mm diameter and a depth of 2 mm, tapped gently to settle and inserted into the detection cell. While solid samples can be measured using FTIR-PAS, the quality of the signal is low compared to powders. For this reason powdered samples tend to be used whenever possible.

2.2 Inside the spectrometer

Both FTIR-Op and FTIR-PAS make use of the same spectrometer: in my case, a Bruker Vertex 70v system. As such, a substantial portion of the procedural details

are the same for both detection methods. The heart of the system is a Michelson interferometer. A schematic representation of the apparatus is shown in Figure 2.1. The following is a description of the operations of the spectrometer up until the sample absorbs the IR radiation and the subsequent detection. The operation of the spectrometer is handled *via* Bruker's OPUS software suite which also facilitates data processing (Section 2.3).

2.2.1 Infrared beam generation

The infrared beam is created by a thermal source (globar) that behaves like a black-body radiator (Figure 2.1A) over the wavenumber region of interest (4000 cm^{-1} to 400 cm^{-1}). The infrared beam enters the Michelson interferometer, which consists of a beam splitter, a stationary mirror and a moving mirror (Figure 2.1B, C and D, respectively). The beam is split into two beams of equal intensity *via* the beam splitter. The beams are reflected back by the stationary mirror and moving mirror. The moving mirror oscillates with a frequency, referred to as the mirror speed, that is set *via* the OPUS control software. By moving one mirror, a path difference is created which causes the beams to interfere with one another. The mirror speed modulates the interference pattern so that the IR frequencies are distinguishable after the Fast Fourier Transform (FFT, discussed in Section 2.3). The specific value of the mirror speed determines the modulation frequency at the wavenumber of a helium-neon laser (15800 cm^{-1}). Suggested mirror speed values are available as presets in the OPUS software, but other values may be input if desired. The direction of mirror movement when collecting data (forward, backward), referred to as the acquisition method, can also be selected.

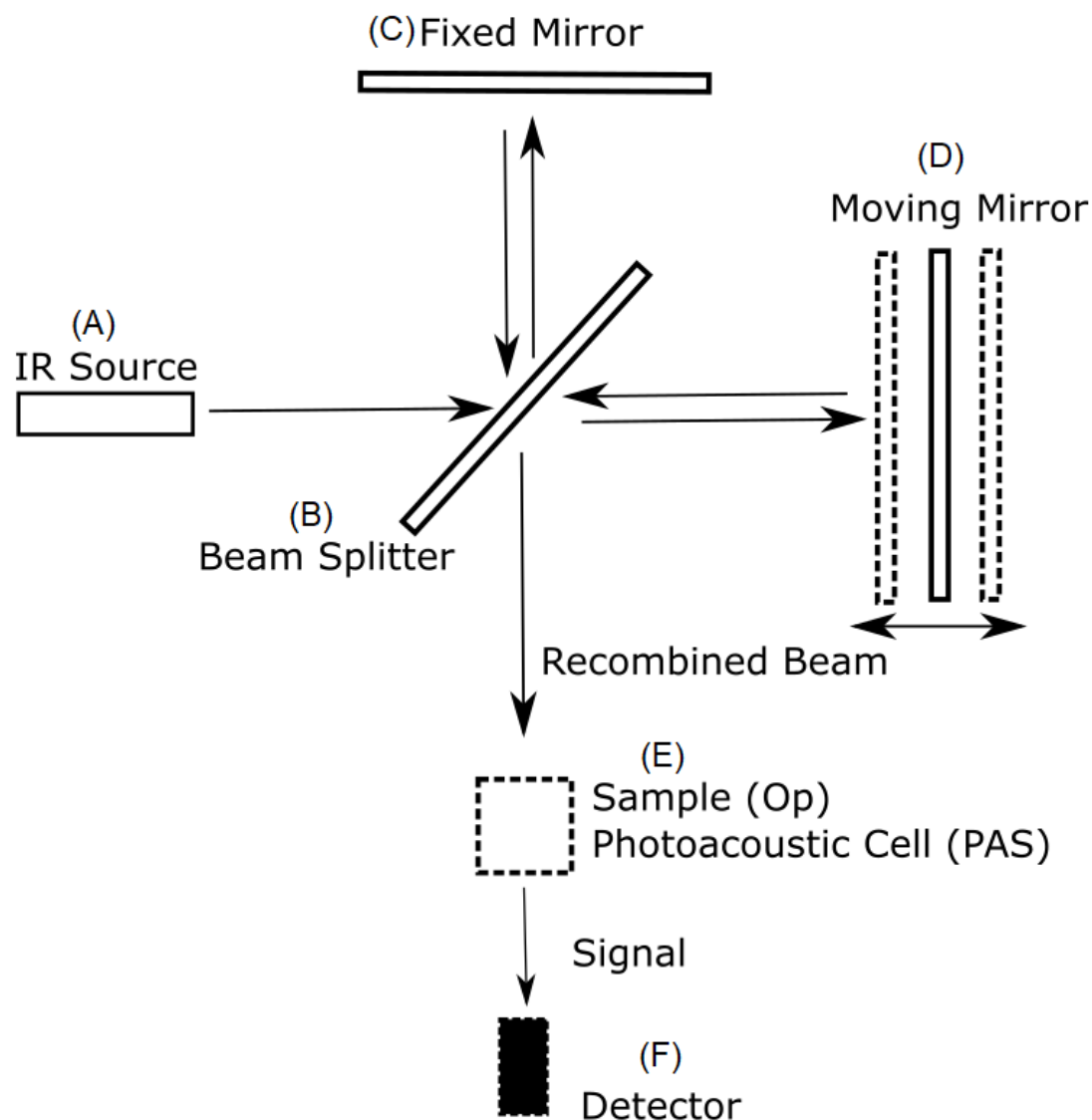


Figure 2.1: A schematic picture of the FTIR spectrometer highlighting the use of a Michelson interferometer. The infrared source (A) generates the initial beam. The beam splitter (B) divides the initial IR beam into two beams with half of the original source intensity. The stationary mirror (C) and the moving mirror (D) are used to create a path difference for the two beams, resulting in interference. After recombining at the beam splitter the IR beam is incident on the sample (E) with the final interferogram being recorded at the detector (F, FTIR-Op) or in the PAS cell (E, FTIR-PAS).

2.2.2 Acquisition method

The user can acquire interferograms in one of three modes: forward, backward or forward-backward. Data taken in either forward or backward mode are then Fourier transformed (following the method outlined in Section 2.3) to produce the FTIR spectrum. Data collected in forward-backward mode is treated as two separate interferograms (one forward, one backward) and transformed individually before being averaged. This is necessary as the forward and backward interferograms have different phase errors and must be phase corrected individually before they can be combined. Data for 100 nm silica particles collected in forward, backward and forward-backward mode (black, red and blue respectively) are plotted in Figure 2.2. The data show that the quality of the spectrum is independent of acquisition method. The spectral intensity has a maximum deviation of less than 1%, located at the 600 cm^{-1} peak. On the advice of our collaborator K. Michaelian, we use forward data acquisition [32]. The reasoning is two-fold. This particular spectrometer (Bruker Vertex 70v) has been shown to have a reduced data quality in some backward acquired data, and a single direction collection allows for a reduced data collection time for a given data point density in the interferogram.

2.2.3 Mirror speed

Figure 2.3 shows data collected using 100 nm silica particles taken at 1.6 kHz (black curve), 2.5 kHz (red) and 5.0 kHz (blue) mirror speeds. From these spectra it is obvious that changing the mirror speed can change the resulting spectra. Reducing mirror speed leads to an increase in overall signal, as expected. This is because slower mirror speeds result in better thermal wave transfer into the carrier gas, leading to higher signal intensities [16]. The thermal diffusion length of the thermal wave in

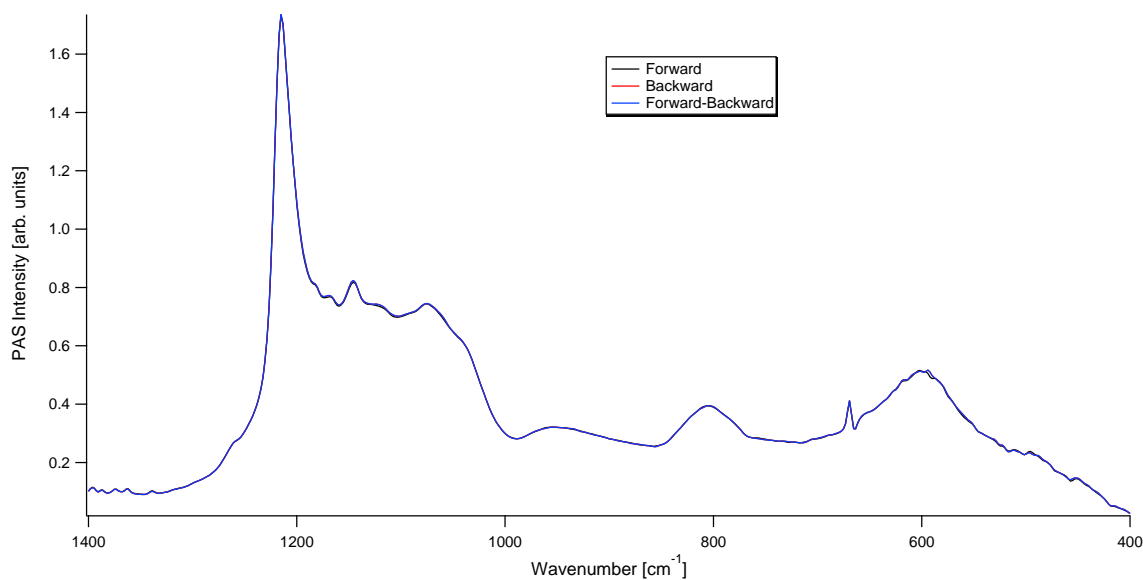


Figure 2.2: Spectra of 100 nm silica particles with different acquisition directions. The spectral data were Fourier Transformed from the backward interferogram (red), forward interferogram (black) and the average of both the forward and backward spectral data (blue). All three acquisition methods produce nearly identical data. Minor deviations in signal intensity are observed around many of the peaks, the largest being the feature at 600 cm^{-1} which is a difference of less than 1% of the intensity.

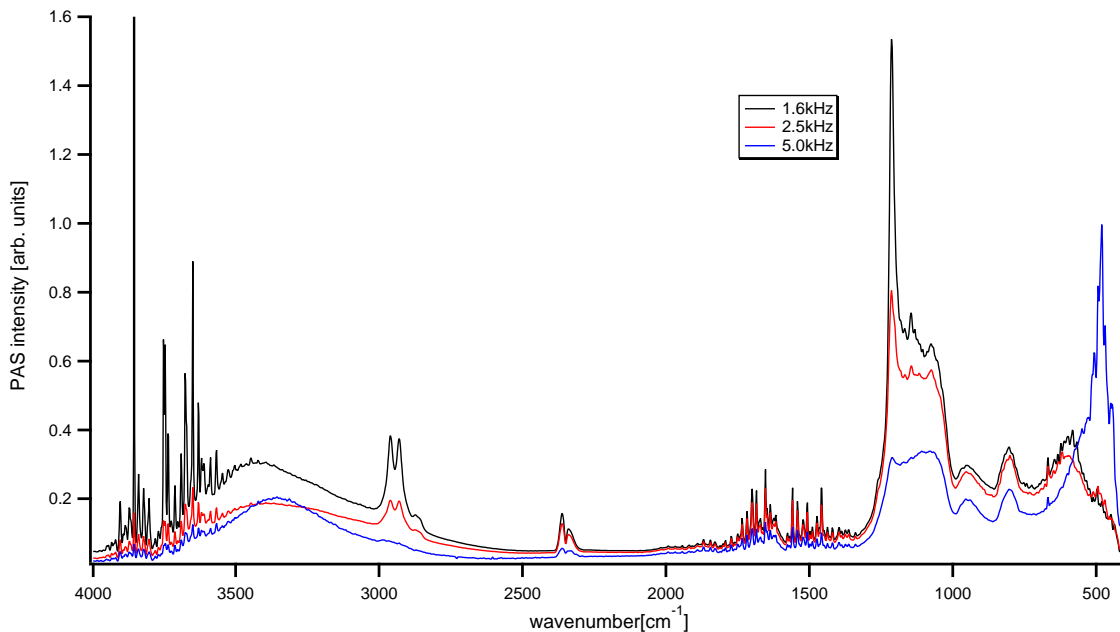


Figure 2.3: PAS spectrum of silica with mirror speeds of 1.6 kHz (black), 2.5 kHz (red) and 5.0 kHz (blue). The slower mirror speed data are in good agreement in terms of peak positions, relative intensities and widths. the 5.0 kHz data shows obvious changes in relative peak heights at 2900 cm^{-1} , 1200 cm^{-1} and 500 cm^{-1} possibly attributed to resonance effects.

the sample is inversely proportional to the modulation frequency, which is set for all wavenumbers by the mirror speed. Lowering the mirror speed increases the thermal diffusion length, resulting in more thermal wave transfer to the carrier gas and thus, more signal detection by the cantilever.

The general peak structures observed in the 5.0 kHz data deviate significantly from the others. This is most easily observed in the low wavenumber region (1400 cm^{-1} to 400 cm^{-1}), where the intensity of the 1200 cm^{-1} peak has been significantly reduced, and there is a sharp increase in signal around 450 cm^{-1} . While the change in average signal intensity was expected, the drastic changes to individual peak intensities was not.

To further investigate the origin of these effects I examined sample data corresponding to an intermediate processing step. These spectra had not been ratioed

against the reference spectrum (carbon black), which is used to correct for instrumentation effects. This type of spectrum is known as a magnitude spectrum and is shown in Figure 2.4a. Reducing the mirror speed results in increased average signal intensity, as it should. Below 1800 cm^{-1} , the peak structure of the signal remains similar, deviating only in absolute intensities. Above 1800 cm^{-1} , the 5.0 kHz data changes shape in relation to the other data sets.

Magnitude data of 250 nm silica particles are plotted in Figure 2.4b as a function of modulation frequency. The modulation frequency for a Michelson interferometer is defined as $f = 2V\nu$, where V is the mirror speed, and ν is the IR frequency [16,33]. A sharp increase in signal detection, referred to as a detector resonance spike, is clearly visible at 800 Hz in both the 2.5 kHz and 5.0 kHz data. While this does not effect the region of interest for the 1.6 kHz or 2.5 kHz data, the resonance causes clear changes to the 5.0 kHz data.

The origin of this resonance effect is not yet reported, but is likely due to the shape of the PAS cell. As expected, the carbon black reference spectrum is also distorted (Figure 2.5). Above 1800 cm^{-1} the 5.0 kHz data deviates from the others significantly due to the PAS cell resonance. The 2.5 kHz reference data has higher signal intensity as compared to both the 1.6 kHz and 5.0 kHz data starting around 2900 cm^{-1} . This is unexpected as slower mirror speeds should produce more signal intensity. Below 1000 cm^{-1} the data sets show changes in relative peak intensities.

The final PAS spectrum (Figure 2.3) is calculated by dividing the magnitude spectrum by the reference spectrum (Figure 2.5). The 1.6 kHz and 2.5 kHz data retain the same peak positions, widths and relative intensities because they are both unaffected in the wavenumber region of interest (4000 cm^{-1} - 400 cm^{-1}) by the cell resonance. The 5.0 kHz data shows clear deviations in relative peak intensities notably in the peak collection centered on 1100 cm^{-1} and in the OH stretching peak

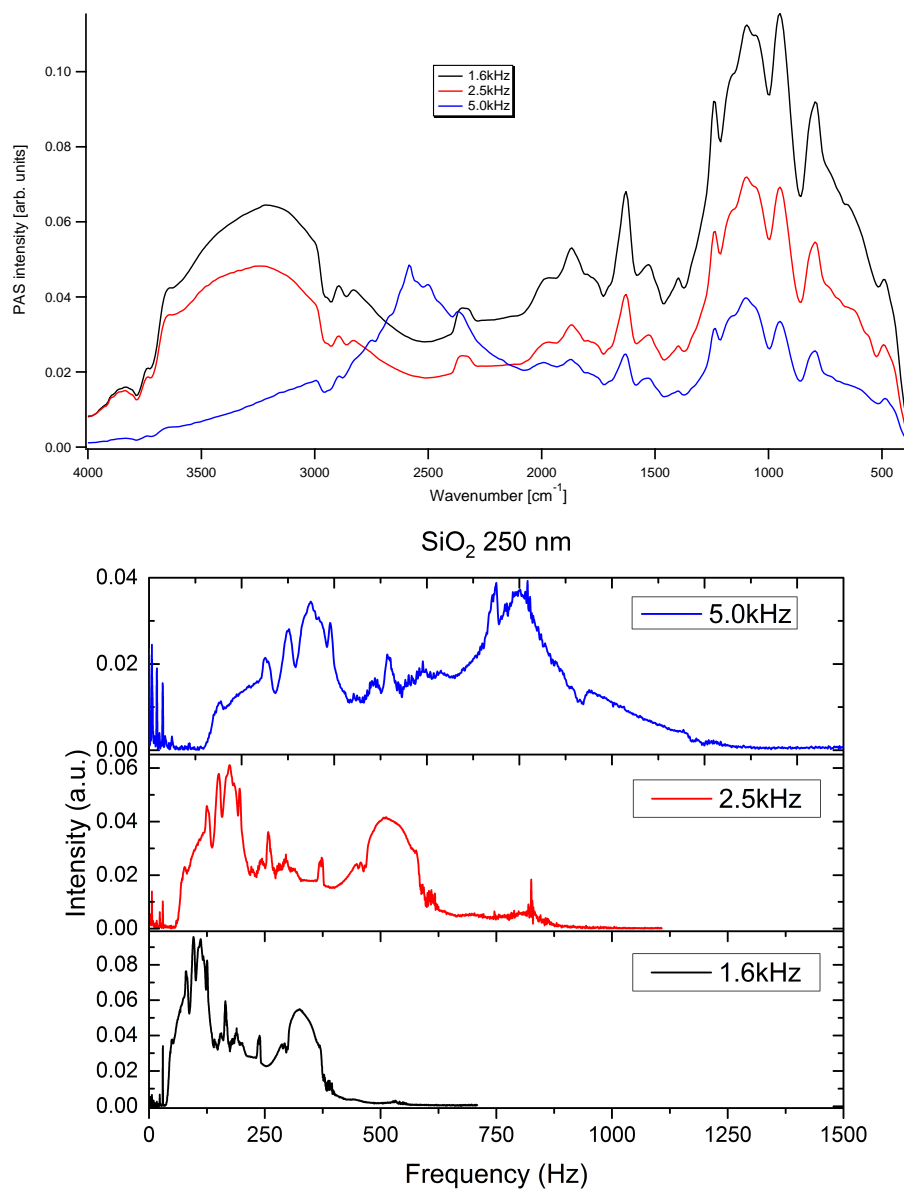


Figure 2.4: (a) Magnitude spectra of 100 nm silica measured with mirror speeds of 1.6 kHz (black), 2.5 kHz (red) and 5.0 kHz (blue). There is a significant change in the peak structures above 1800 cm^{-1} in the 5.0 kHz data. Below this peaks maintain shape and position, with higher intensities at slower speeds. (b) The mirror speed is adjusted (5 kHz, 2.5 kHz and 1.6 kHz) for 250 nm silica particles, plotted as a function of modulation frequency. The resonance peak around 800Hz is a feature of the photoacoustic cell. The resonance spike causes the 5 kHz data to diverge significantly from the others. Plots created by collaborator K. Michaelian (NRC CanmetENERGY, Edmonton) using my data.

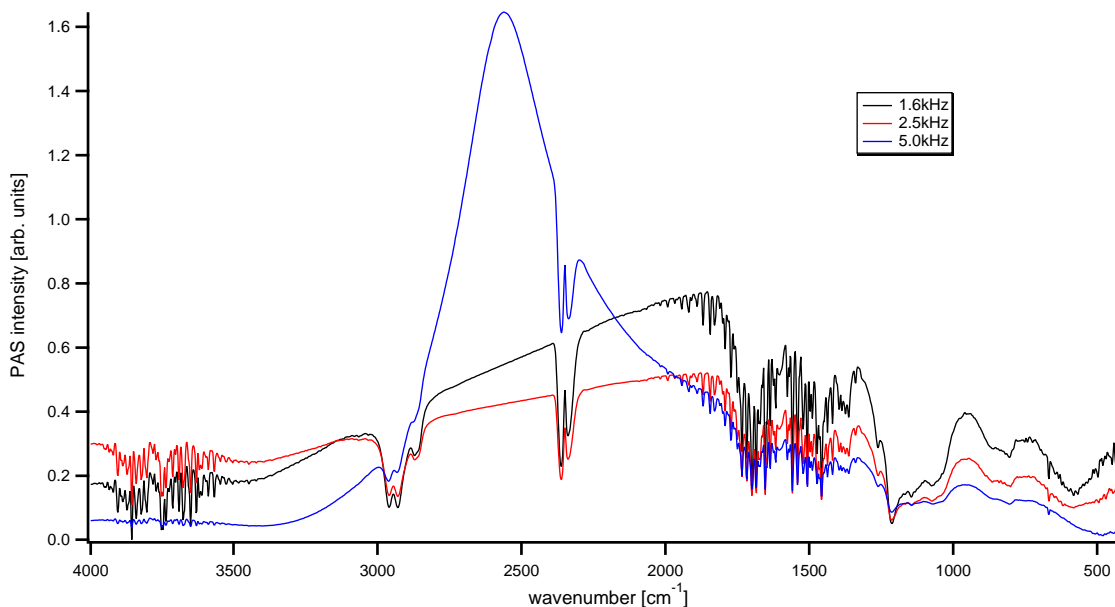


Figure 2.5: Magnitude plots of the carbon black reference sample measured with mirror speeds of 1.6 kHz (black), 2.5 kHz (red) and 5.0 kHz (blue). As with the silica sample shown in Figure 2.4a there is a change to peak shapes above 1800 cm^{-1} using a mirror speed of 5.0 kHz.

around 2900 cm^{-1} .

The addition of a sharp peak at 500 cm^{-1} is interesting. In this region of the spectrum the spectrometer optics begin to absorb the IR light, causing a sharp drop in the signal intensity in both the sample signal and the reference (Figures 2.4a and 2.5, respectively). The reference spectrum loses signal more rapidly. This results in the appearance of the feature at 500 cm^{-1} in the corrected spectrum (Figure 2.3). It is unclear to us currently why the carbon black data was affected so much more than the silica in this region. Silica spectral peaks of interest do not appear in this wavenumber region so, for our purposes, this can safely be ignored.

2.2.4 Co-additions

The signal-to-noise ratio (SNR) of a measurement taken using either detection method is easily improved by increasing the number of co-added scans. Figure 2.6 shows the PAS signal of 100 nm silica particles measured using 4 scans (black) and 128 scans (blue). It is clear that the SNR has been significantly improved, resulting in a higher quality spectrum. Larger spectral features such as the sharp peak near 1200 cm^{-1} or the broad peak around 800 cm^{-1} show little change in peak shape with increasing co-additions. Peak positions remain unchanged but there is an overall loss of intensity with increasing co-additions. It is possible that this is related to minor shifts in the point of maximum intensity in the recorded interferogram. Averaging over successive interferograms could result in a reduced absolute intensity which, following the Fourier Transform, would lead to a reduction in signal. Finer details, such as the peak near 660 cm^{-1} gain more obvious structure by increasing the co-additions. While this increase in quality may not be necessary for qualitative comparisons such as sample identification, it is a crucial step for any quantitative analysis. Positions, widths and intensities of fitted peaks have been used to identify structural disorder [25].

Also worth noting is that the time required for data collection involving 128 co-additions is on the order of 15 minutes. FTIR-Op would be able to produce high quality data in much less time because of the much higher mirror speeds used in that detection method. This is possible because the IR light absorbed by the sample is detected directly. FTIR-PAS signal requires the transfer of thermal energy from the sample to the carrier gas which requires more IR absorption to produce a detectable signal.

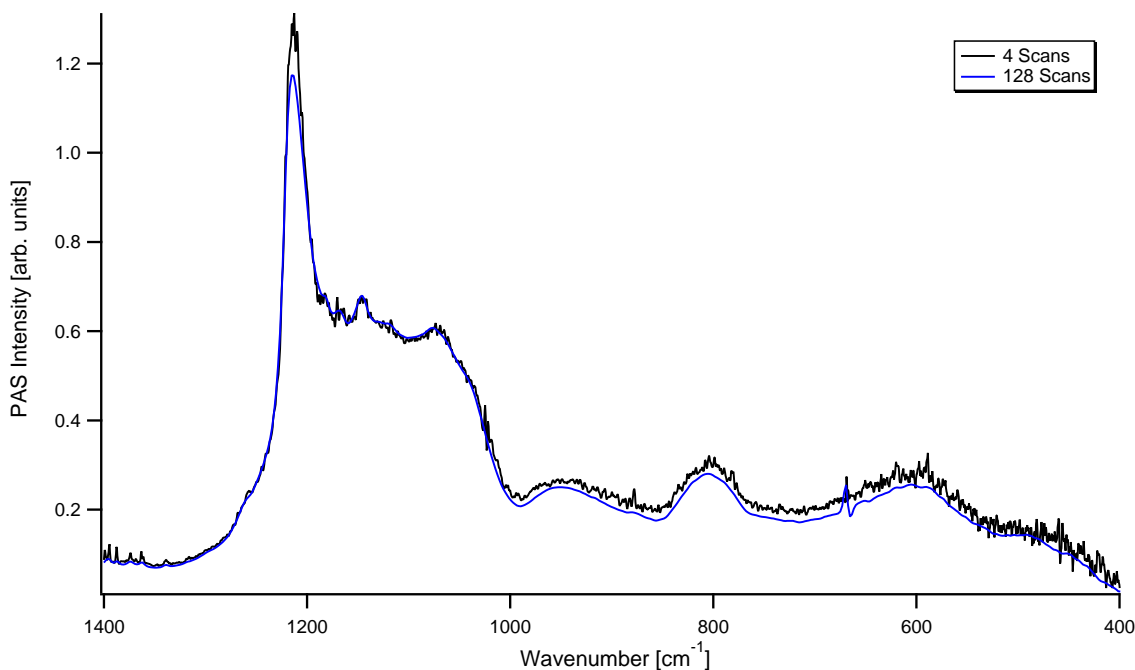


Figure 2.6: FTIR-PAS spectrum of 100 nm silica particles using 4 scans (black) and 128 scans (blue). The increase in co-additions results in a higher signal-to-noise ratio. There is an overall loss of intensity with increasing co-additions.

2.2.5 Detection of IR absorption by the sample

The recombined beam is directed at the sample (Figure 2.1, part E). The detection of absorbed IR radiation varies between FTIR-Op and FTIR-PAS. The processes are outlined below. Regardless of detection geometry, the resulting experimental data are stored as interferograms (intensity *vs.* mirror displacement). One of my typical interferograms contains 14732 points; Figure 2.7 shows the central 1000 points for a 250 nm silica particle PAS experiment.

2.2.5.1 FTIR-Op

For FTIR-Op, the sample is in the form of a diluted KCl pellet directly in the beam path. The material within the pellet absorbs IR radiation corresponding to its characteristic vibrational modes. The remaining IR beam is incident on a detector (Figure

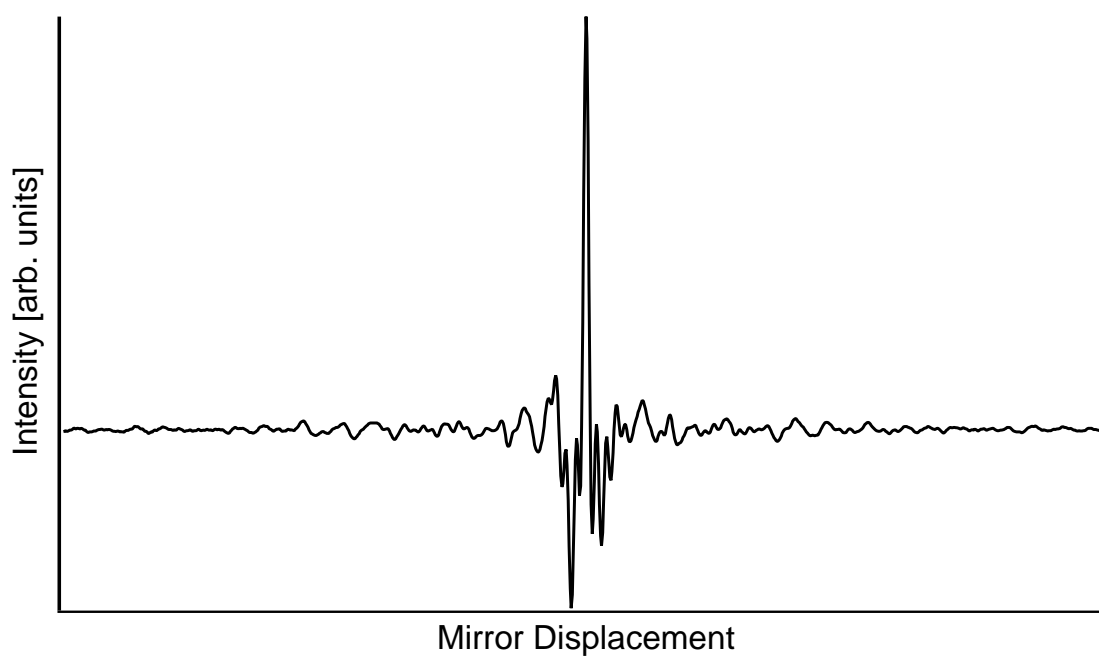


Figure 2.7: Center region (1000 of 14732 points) of a double-sided interferogram recorded from a FTIR-PAS experiment using 250 nm silica particles. The interference of the IR beams causes regions of high and low intensity as the mirror displacement changes.

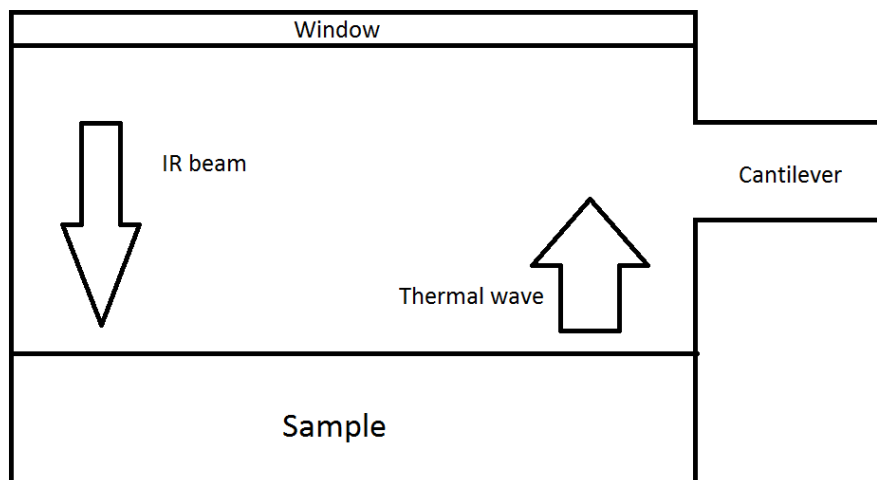


Figure 2.8: A schematic picture of the photoacoustic cell. The interfered IR beam enters the cell, and is incident on the sample. This causes thermal expansion/contraction in the sample, giving rise to a pressure wave in the carrier gas. The pressure wave is detected by the cantilever and saved as an interferogram.

2.1, part F) and recorded as an interferogram.

2.2.5.2 FTIR-PAS

For my FTIR-PAS experiments, the location marked E in Figure 2.1 is a Gasera PA-301 photoacoustic cell. A schematic diagram of the photoacoustic cell is shown in Figure 2.8. The beam is redirected into the cell and onto the powdered sample where it absorbs the modulated radiation and heats up. This heating leads to an expansion-contraction cycle of the sample, which is in contact with the carrier gas inside the photoacoustic cell. A pressure wave is transmitted *via* the carrier gas to the cantilever detector. The cantilever deflection is measured using a laser. This deflection signal is recorded as an interferogram (intensity *vs.* mirror displacement) and is specific to the sample measured.

2.3 Data processing

To obtain a spectrum, the interferogram is Fourier transformed. This procedure is identical for an interferogram collected either in FTIR-Op or FTIR-PAS. The transform is done in many steps, all of which are important for the quality of the final product. The instrumentation introduces phase errors in the interferogram. The Fourier transform procedure incorporates a method to adjust for these errors known as a phase correction. The following procedure is based on the pictorial essay laid out by Griffiths and de Haseth [33]. It has also been reproduced by the FTIR software company Essential FTIR and is hosted online [34]. In that spirit, each step in the process is accompanied with an image to show how the process is affecting the data visually. My procedure incorporates the Mertz phase correction method [35,36].

2.3.1 Preparing for the Fast Fourier Transform

There are two important steps that must be taken prior to application of the Fast Fourier Transform (FFT) algorithm: normalization and zerofilling. Depending on the reference material, these may be considered part of the algorithm or not. In the interest of clarity and transparency, they are included here as preparation steps.

The process begins with the interferogram obtained by FTIR-Op or FTIR-PAS detection (Figure 2.9). First, the data is normalized by subtracting the average value of the data set (red line) from each datum. This brings the baseline of the data to zero, which is required to eliminate discontinuities created when the data is zerofilled.

The importance of zerofilling the data is two-fold. Firstly, the computational efficiency of FFT algorithm is higher when the number of input data is a power of 2 [33]. Secondly, the output of the FFT algorithm is two data arrays corresponding to the real and imaginary spectral data. The size (number of points) in each of these

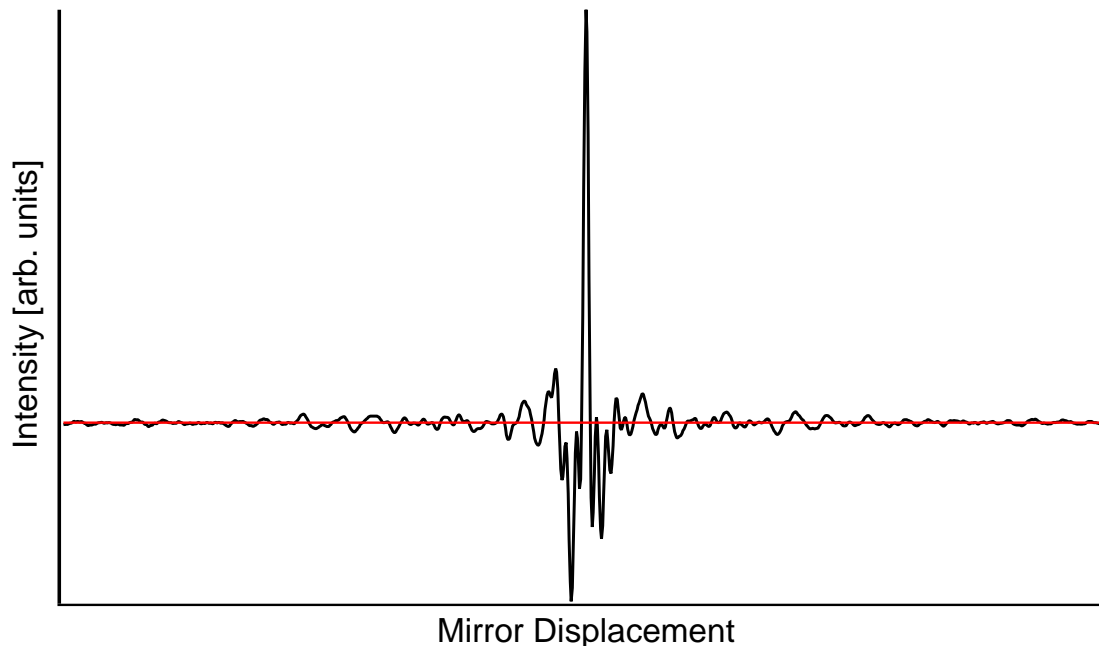


Figure 2.9: Center region (1000 out of 14732 points) of an unprocessed interferogram (intensity *vs.* mirror displacement). The red line is mean of the data set. The interferogram is normalized *via* mean subtraction from each datum.

arrays is half the number in the input array. Given an input data set of size N , the real and imaginary data sets will each contain $\frac{N}{2}$ data points. Zerofilling the interferogram data results in interpolations between data in the real and imaginary arrays, smoothing the final result without losing spectral information [33]. As the name suggests, zerofilling is accomplished by padding the input interferogram data with zeros up to a desired size. For computational efficiency this will bring the number of data points in the interferogram to a power of 2 (See Figure 2.10). The exact amount of zeros added will depend on the desired level of data interpolation.

The N data are zerofilled with $2^{(m-1)}N$ zeros, where m is the zerofilling factor. As mentioned previously, this results in an interpolation between data points in the output arrays. I used a value of 2. Values higher than this result in further interpolation between the linearly independent points, which would produce smoother curves

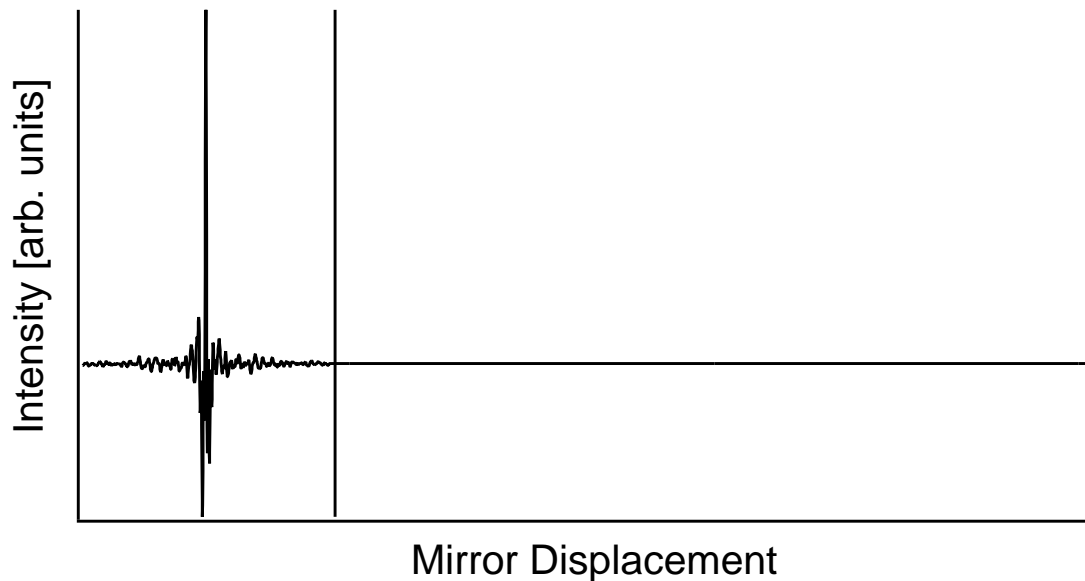


Figure 2.10: The normalized interferogram. Vertical lines mark the next power of 2 and the number of points which marks a zerofilling factor of 2.

but no further information is gained [37].

2.3.2 Phase correction

An idealized experimental setup would produce interferograms with no phase errors. Phase errors are introduced to the interferogram by the instrumentation and need to be accounted for when converting the signal from an interferogram to a spectrum.

The phase correction marks the last stage in the process prior to the application of the FFT algorithm. Coupled with the phase correction is the choice of apodization (windowing) function. Strictly speaking, windowing could be considered a step on its own, as data possessing no phase errors would still need to be apodized. The Mertz multiplicative phase correction method also makes use of the selected windowing function.

A subset of the data centered on the Zero-Path Difference (ZPD) is extracted (referred to as the centerburst, Figure 2.11), from the normalized, zero-filled inter-

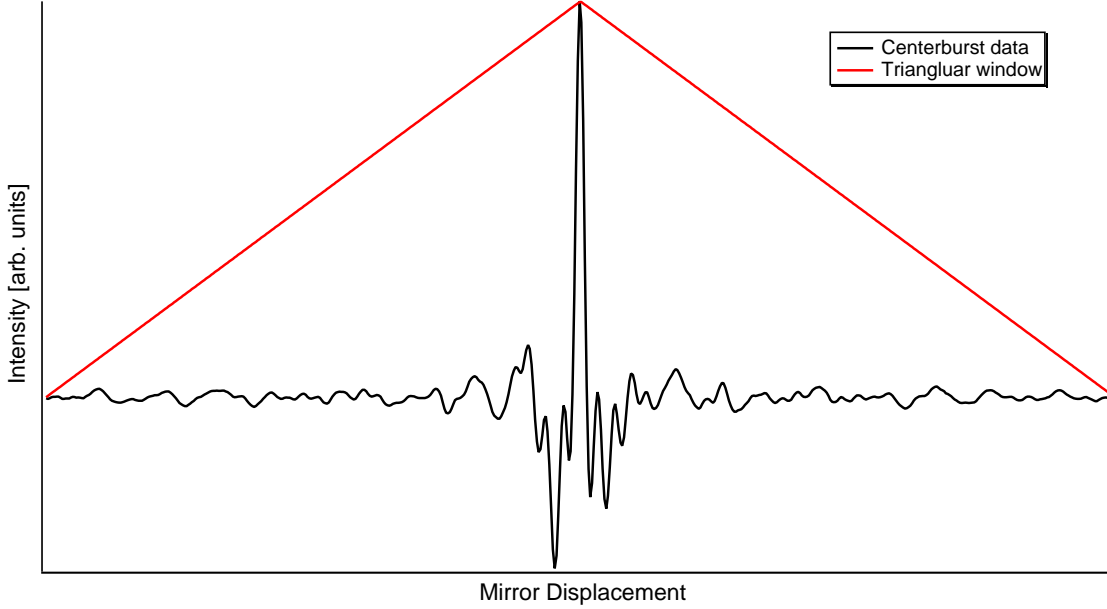


Figure 2.11: The centerburst data subset that will be used to prepare the phase correction data. A basic triangular window function is overlaid. The two will be multiplied together during apodization.

ferogram. The amount of data points used depends on the desired phase resolution. The highest this should be is twice the spectral resolution. In practice, such a high resolution phase spectrum is rarely needed. The value of the phase resolution is set in the OPUS control software. The software decides how many data points are to be used to calculate the phase correction data based on the phase resolution. It is not immediately obvious to the software user how many points would be used, as it depends on the the distance (microns) between successive data points in the interferogram, which is half the wavelength of the He-Ne laser ($0.3164 \mu\text{m}$). This can be calculated approximately according to the equation:

$$\text{res} \approx [(N - CB)\frac{1}{2}\lambda_{\text{HeNe}}]^{-1}, \quad (2.1)$$

where N is the number of data points in the interferogram, CB is the data point corresponding to the centerburst and λ_{HeNe} is the wavelength of the He-Ne laser [17].

The centerburst data are apodized by a windowing function set within the OPUS control panel prior to runtime. The window is a function designed to fall to zero at the beginning and end of the data set (see Figure 2.11). A window function is applied to the data set in an effort to reduce “leakage” aberrations in the FFT output that are introduced with sudden changes to the data (discontinuities) [38]. Without apodization, the FTIR spectrum would likely contain numerous leakage aberrations, many of which may be indistinguishable from true spectral features.

Figure 2.12 demonstrates the effect of windowing prior to Fast Fourier Transformation. A simple signal composed of two sine functions (black) is Fourier transformed using the FFT algorithm. This results in many ripples in the frequency domain caused by the discontinuities at the beginning and end of the signal. The original signal (black) is multiplied by the Blackman-Harris 3-Term windowing function (blue) resulting in the data at the bottom left (red). After applying the FFT, the frequencies of the sine functions are recovered without the leakage aberrations previously observed.

The simplest window would be a triangular function with a value of 1 at the ZPD and zero at the beginning and end. Other window functions have been developed, and are included in the OPUS software as standard. The Blackman-Harris 3-Term window was the default window setting in the software. After the apodization, the data are zero-filled to have the same number of data points as the original zero-filled dataset.

The apodization (windowing) function used in the FFT procedure discussed previously was found to have a negligible effect on the final spectrum. Three different windowing functions were used to transform the same interferogram for 100 nm silica particles (Figure 2.13). The different window functions result in nearly identical spectra. The triangular window showed the largest difference from the other functions

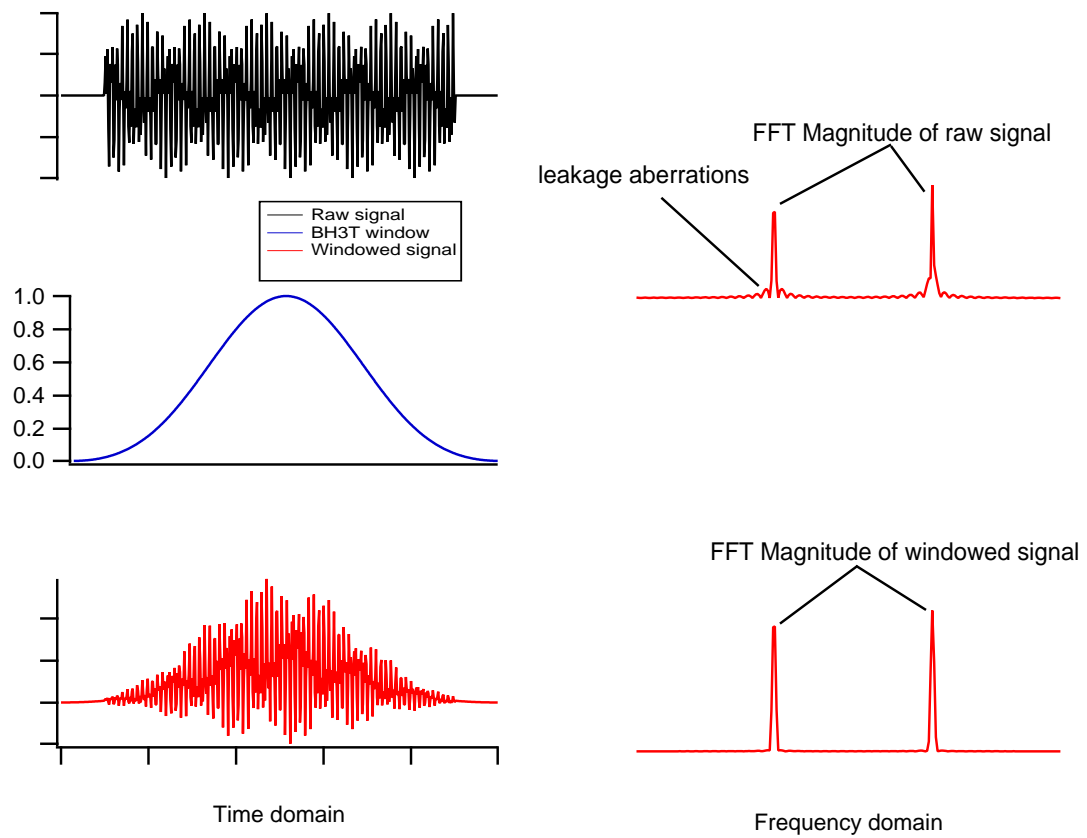


Figure 2.12: A computer generated signal comprised of two main frequencies (black) and the output of the FFT algorithm. Leakage aberrations are indicated. The same generated signal is multiplied by a Blackman-Harris 3-Term window function (blue) before applying the FFT algorithm. By windowing, nearly all of the leakage aberrations have been removed. Figure is adapted from Ref. [2].

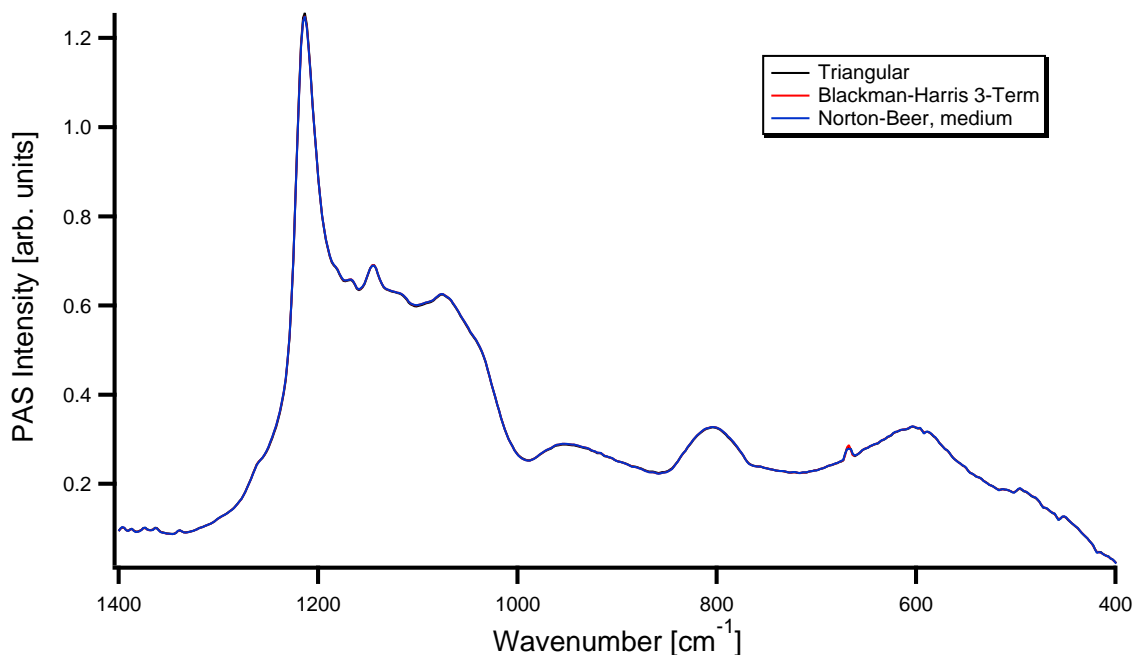


Figure 2.13: Changing the window function used in the FFT procedure results in negligible changes to the output spectrum. Three different windowing functions were used: Triangular (blue), Blackman-Harris 3-Term (black) and Norton-Beer, Medium (red).

of 0.3% change in peak intensities. The Blackman-Harris 3-Term and Norton-Beer (medium) options show only a 0.1% difference in peak intensity. The windowing has no effect on the peak positions, widths or relative intensities. As this effect presents in all peaks, it can be safely ignored for quantitative comparisons of relative peak heights.

The interferogram is rotated such that the data before the centerburst are placed at the end (Figure 2.14). This results in a data set that begins with the ZPD, falls to zero for the majority of the middle region and ramps back up to near the ZPD value at the end. This data set is Fourier Transformed to produce the real, $R(\nu)$, and imaginary, $I(\nu)$, components (Figure 2.15). From this the phase angle is calculated at every wavenumber according to the relationship:



Figure 2.14: The apodized, zero-filled centerburst data is rotated such that the data prior to the centerburst are placed at the end.

$$\theta(\nu) = \tan^{-1} \left(\frac{I(\nu)}{R(\nu)} \right). \quad (2.2)$$

The original interferogram is treated similarly: apodization, rotation and Fourier Transformation. The phase corrected spectrum is calculated from the real and imaginary data, and the phase angle according to the following equation:

$$S(\nu) = R(\nu) \cos(\theta(\nu)) + I(\nu) \sin(\theta(\nu)), \quad (2.3)$$

where θ is the phase angle calculated by Equation 2.2 [36]. The magnitude spectrum is shown in Figure 2.16.

The choice of phase correction method can have a non-negligible effect on the spectrum produced. Bruker's OPUS software package has many built in options; I examined the Mertz [35] and power spectrum (modulus) phase corrections. Figure 2.17 shows the FTIR-PAS spectra for 100 nm silica particles using different phase

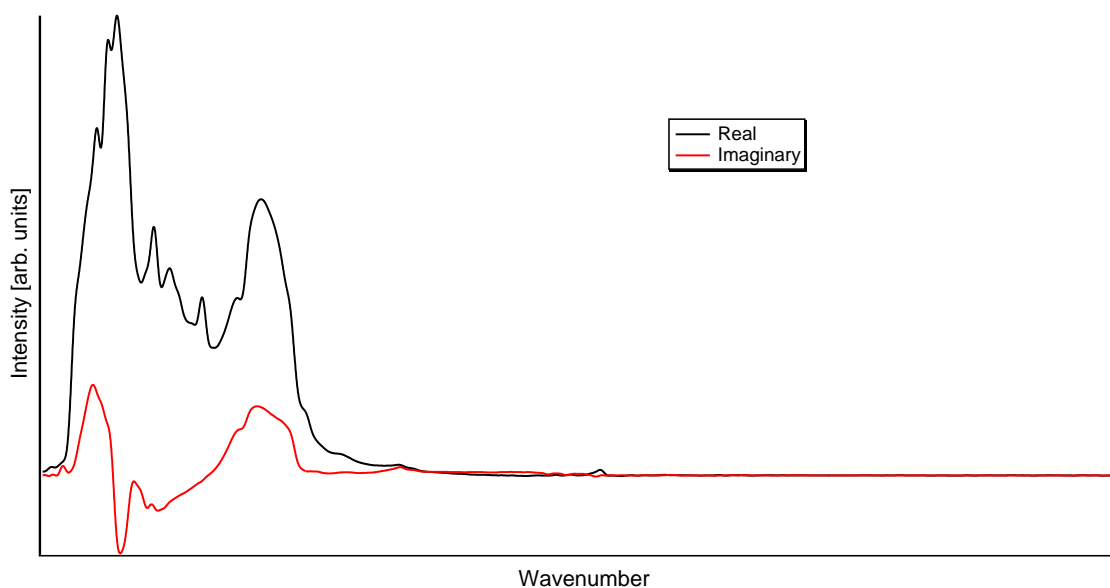


Figure 2.15: The Real and Imaginary component results of the FFT algorithm on the manipulated centerburst data. The phase angle is calculated from these arrays according to Equation 2.2

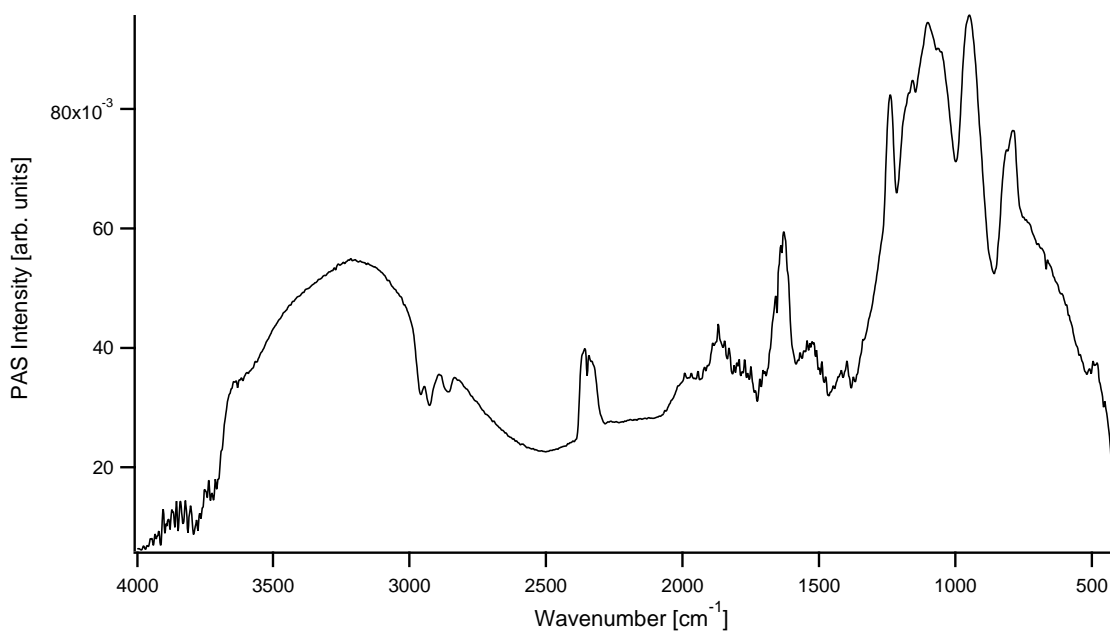


Figure 2.16: Magnitude spectrum produced as the final result of the phase corrected, Fourier transformed interferogram. Using the phase angle calculated by Equation 2.2, this result is produced from Equation 2.3.

corrections. The green line was calculated using the power spectrum correction while the black employed the Mertz method. All prominent spectral features are observed in both phase corrections. Peak widths remain unchanged but there is minor shift (approximately 2 cm^{-1}) in peak positions for all features. A wavelength-dependent average intensity effect for the modulus method leads to reduced signal at the lower wavenumbers.

Our collaborator K. Michaelian recommends the Mertz phase correction. The modulus correction can result in the presence of non-sample related peaks in the spectrum caused by rectifying noise in the interferogram during the phase correction. However, I observed no additional peaks in the power spectrum treatment of these SiO_2 data.

2.3.3 Signal Correction

The final spectrum is created by correcting for the background signal of the experimental setup. In the case of FTIR-Op, the background signal is an open beam in vacuum. For FTIR-PAS the background is a highly absorbing reference sample (carbon black standard, Gasera). The final spectrum is produced by dividing the sample spectrum by the background spectrum. An example of the two signals (sample and reference) for FTIR-PAS are shown in Figure 2.18.

2.4 Best practices

It is clear that there are many variables that can be manipulated while producing an FTIR spectrum. Examined in this thesis are the mirror speed, acquisition method, number of co-additions, windowing function and phase correction method. These parameters are varied to observe the effect on the spectrum in an attempt to distinguish

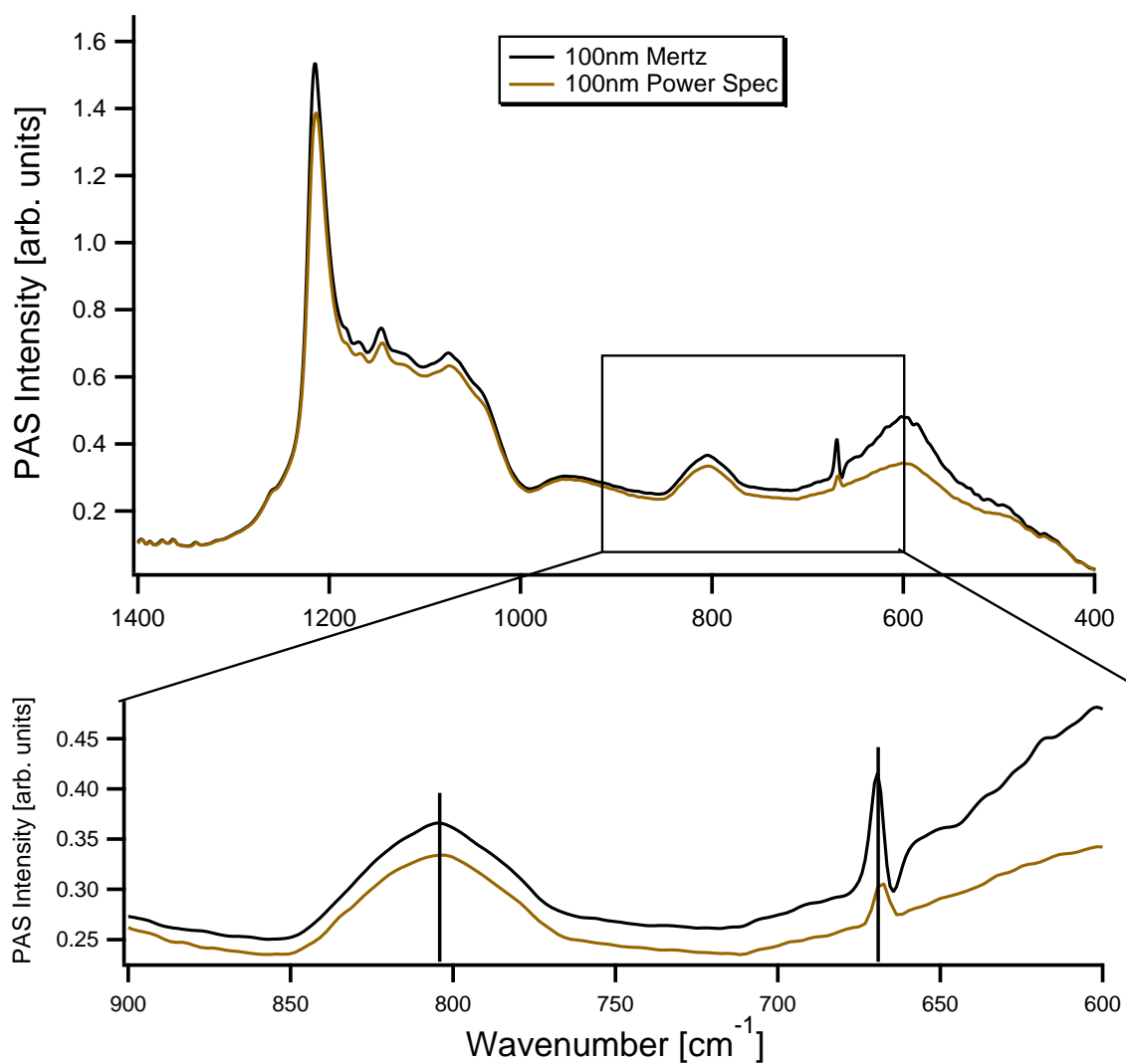


Figure 2.17: FTIR-PAS spectrum of 100 nm silica spheres using the Mertz (black) and modulus (green) phase correction methods. A wavelength dependent intensity difference is observed at lower wavenumbers. Peak widths remain unchanged between the correction methods, while peak positions shift approximately 2 cm^{-1} .

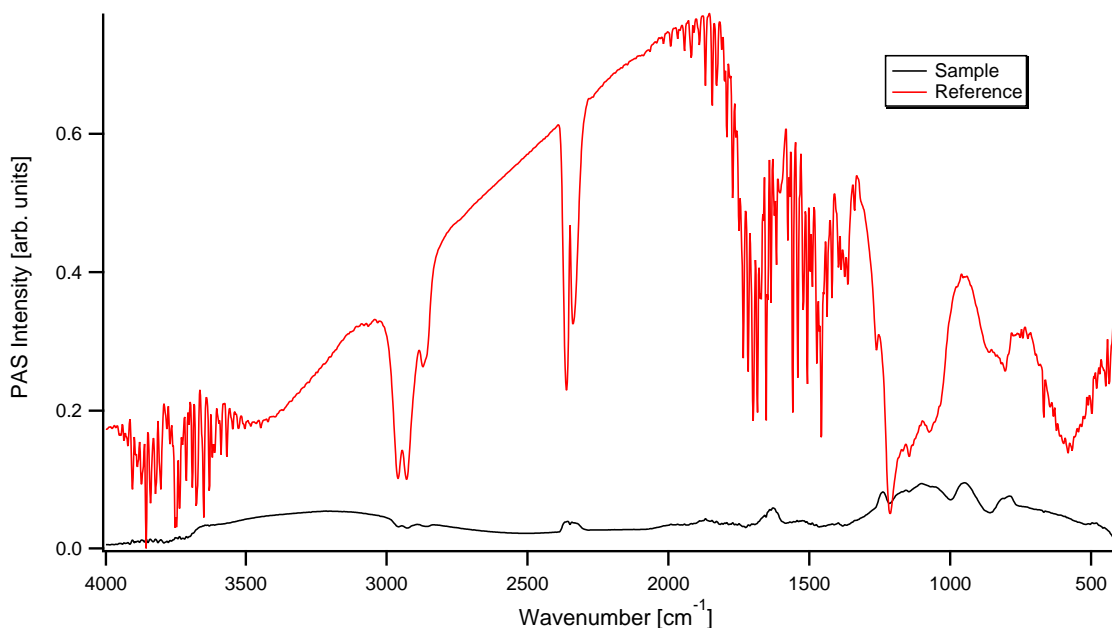


Figure 2.18: FTIR-PAS spectrum of the sample and reference. Background correction is accomplished by dividing the sample by the reference.

what spectral changes are caused by sample differences, which are caused by these parameters and most crucially, if they can be ignored when comparing spectra taken with different initial parameters.

This investigation of experimental parameters highlights some of the possible pitfalls that one may experience when operating a commercial FTIR spectrometer as-is. The results of these experiments suggest that to obtain high quality data that the experimenter can have reasonable confidence in, certain settings should be respected.

The mirror speed should be chosen carefully with respect to the experimental setup. Our use of the Gasera PA-301 photoacoustic cell necessitates that our mirror speed be set to less than 2.5 kHz to avoid distortion of the spectrum by resonance effects. The added benefit of reducing the mirror speed is that the signal intensity of the sample defining features will increase. The thermal diffusion length is inversely related to the modulation frequency (mirror speed), so by reducing the mirror speed,

we are increasing the thermal diffusion length resulting in an increase to the amount of signal transferred from the sample to the detector as a pressure wave in the carrier gas [16, 39].

The phase correction used should also be carefully considered. The Mertz correction is superior compared to the modulus phase correction based on the reasons given previously [32]. Also worth considering is the wavelength dependent intensity differences between the two methods. For our purpose this favors the Mertz method as higher intensity in the lower wavenumber region is desirable for studies concerned with lattice modes, as these lower energy vibrations appear here.

Many of the parameters were shown to have little effect on the final spectrum. The windowing functions tested were: triangular (Bartlett), Blackman-Harris 3-term and the Norton-Beer (medium). The data shows no relevant changes to the characteristics of interest (peak positions, widths and relative intensities) when any of these apodization options were selected. The different acquisition directions of the interferogram also showed only minor differences in the final spectrum but for the reasons laid out in Section 2.2.2, I recommend forward direction acquisition given an identical setup. This results in a reduced data collection time for a given density of data points in the interferogram and avoids the possibility of poor backward data. The choice of co-additions used will affect the SNR. I chose a value for co-additions that yielded quality data in an acceptable amount of time with our Bruker Vertex 70v system and Gasera PA-301 photoacoustic cell.

With these ideas in mind, one can also consider spectral comparisons between data collected with different conditions. The best case would be data that is stored as raw interferograms and thus, may be re-processed with a different phase correction. The mirror speed and the co-additions (SNR) will be set at runtime however, and thus cannot be changed.

Literature related to both FTIR-Op and FTIR-PAS is often published without indicating many of these parameters [13–15,18,19,40]. The data I have discussed suggests that the inclusion of these collection and processing parameters is important, as differences among data collection procedures can lead to spectral differences that otherwise many not be properly accounted for. The classic use of fingerprint identification FTIR would not benefit greatly from its inclusion, but the same cannot be said for more quantitative analyses. For those concerned with precise peak positions, widths and relative intensities, reporting of these data acquisition parameters would allow for better comparisons among the community and ultimately strengthen the technique as a whole.

Chapter 3

Using best practices

By investigating the effects of the experimental parameters outlined in Chapter 2, I was able to identify sources of spectral artifacts related to the instrumentation, the data collection procedures and the data processing. The use of any FTIR-PAS spectrometer setup as a blackbox piece of equipment is adequate for sample identification studies, but falls short when seeking to extract further information from the data. The usefulness of FTIR-PAS can be enhanced by restricting further experiments to these idealized practices highlighted in Section 2.4. With this in mind, I collected new data for the monodisperse silica particles using these criteria. The particle sizes are interesting, as they fall roughly an order of magnitude below the smallest wavelength of light used ($2.5 \mu\text{m}$), which results in the observation of only surface modes in the IR spectrum [41]. The purpose of this was twofold:

1. Other researchers have previously reported noticeable effects on relative peak intensities in other FTIR detection schemes related to particle size [42] and,
2. Size effect studies on FTIR-PAS have yet to explore the regime of these particle sizes (100 - 1000 nm) [39, 43–46].

3.1 Experimental details

3.1.1 Silica spheres

The amorphous silica samples used in this investigation were AngströmSphere silica spheres purchased from Fiber Optic Center (New Bedford, MA, USA) in sizes of 100 nm, 250 nm, 500 nm and 1000 nm. The particles present as a white, free flowing dry powder.

The availability of controlled size manufactured particles allowed for the continued investigation of particle size effects in a regime that had not been explored. The choice of monodisperse SiO_2 particles was made in an effort to more definitively identify trends related to changing particle size without the need to consider particle size distribution effects, as was done in previous investigations using SiO_2 [39, 43, 44]. While other monodispersive samples, such as polymer beads of varied chemical composition, are commercially available, I chose silica because of previous expertise in the Poduska group [4]. Silica produces a relatively simple spectrum with clearly defined vibrational modes in the mid-IR region. However, the use of amorphous silica resulted in a spectrum that is not easily used for quantitative analysis. Amorphous materials result in broad, rounded peaks that are challenging to fit with traditional Gaussian or Lorentzian fitting algorithms.

3.1.2 Photoacoustic measurements of silica

All experiments were executed using the previously discussed best practices (See Section 2.4). For reference, the relevant parameters are listed here.

- 4 cm^{-1} wavenumber resolution
- Forward-direction acquisition

- 1.6 kHz mirror speed (5.0 kHz for FTIR-Op)
- 128 co-additions
- Blackman-Harris 3-Term apodization function
- Mertz phase correction
- 16 cm^{-1} phase resolution
- Zerofilling factor of 2

Spectra for the monodisperse silica spheres were collected with a Bruker Vertex 70v spectrometer fitted with a PA-301 photoacoustic cell attachment (Gasera Inc). A carbon black standard (Gasera, Inc.) served as a background reference. A small (approximately 60 mg) amount of silica was placed into the sample cup (10 mm diameter, 2 mm depth) such that the entire bottom of the cup was covered but no so much as to reach the top of the cup when leveled by tapping the cup gently on the table. The sample cup was then placed in a sample holder which was inserted into the cell.

FTIR-PAS experiments were done in open air. When the sample is exposed to the IR beam, specific wavelengths are absorbed corresponding to the characteristic molecular vibrations of the sample. This causes thermal energy transfer from the sample to the surrounding carrier gas (open air). The thermal transfer generates pressure waves in the air which are detected by the deflection of a cantilever within the cell. The Fourier Transform of the lever deflection is the photoacoustic signal. The sample spectrum is then the ratio of the sample signal to the carbon black reference signal.

3.1.3 Transmission measurements of silica

Optical grade potassium chloride (KCl) powder was ground with a mortar and pestle to a fine dust. Each of the silica samples were carefully mixed, individually, with KCl dust to disperse the silica throughout the mixture. The mixture was placed into a 5mm pellet die and pressed into a semi-translucent pellet with an approximate thickness of 0.5 mm using a Pike Technologies hand press. A background spectrum of the IR beam was taken with an empty sample compartment under vacuum to match the conditions of the sample-pellet spectrum. The sample compartment was vented before KCl-silica pellet was placed in the beam path. By performing the data acquisition under vacuum, water and carbon dioxide are removed from the beam path.

FTIR-Op spectra of the samples were calculated by the OPUS software suite which also controls the instrument. Both the background and the sample measurements were recorded as interferograms individually. Using the pre-defined parameters listed at the beginning of this section, the software took the Fourier Transform of each signal using the same type of method outlined in Section 2.3. This produced single channel signals of both the background and the sample. The FTIR-Op spectrum is calculated by division of the sample data by the background.

3.2 Motivation

We selected monodisperse silica spheres as a test case to differentiate between sample effects and instrumentation artifacts. Particle size effects as they relate to FTIR-PAS have long been at the forefront of related research [18, 40, 43, 44, 46, 46, 47]. While some groups focused on monodisperse particles [39], other investigations centered on sizes defined by mean-size distributions [43, 45, 46]. Investigations of size were the beginnings of PAS studies as applied to particulate materials [48]. I sought to

continue this trend; investigating particle size effects for sub-micron sized particles.

I used silica due to the availability of various sizes with a high degree of size control. Based on previous reports related to FTIR-PAS and size effects, we expected that smaller particle sizes should produce more signal intensity overall, with no observed changes to peak widths or relative intensities. It was reported that decreasing particle size leads to an overall increase in signal intensity [39, 43–45]. This was attributed to the increases porosity in the powdered samples. The increase in the porosity results in a larger surface area in contact with the carrier gas. This increase in surface area results in more thermal wave transfer from the sample into the carrier gas, which will be observed as an increase in overall signal. Silica particles used in those studies where particle distributions characterized by mean particle size. The size averages were generally in the few to few-hundred micron range, which is much longer than the 0.1 - 1 μm particles used in my thesis work.

Research related to other FTIR detection schemes (Attenuated Total Reflection, ATR) suggested that particle size changes result in shifts the relative peak intensities [42]. Selecting sizes in the sub-micron range was beneficial to us because it bridged the existing gap in the FTIR-PAS silica size dependence literature that had previously been unexplored, while simultaneously extending the range tested in the other FTIR detection schemes that showed relative peak intensity changes related to particle size.

Based on the thermal properties of silica, the thermal diffusion length of the PA signal was an order of magnitude lower than the largest particle size (1000 nm). From this, it was expected that there should be no differences in where the PA signal was generated within the sample, as the signal should have been generated at the surface rather than within the bulk. The dominating effect related to the particle size change should be the changing porosity leading to differences in overall signal intensities [45].

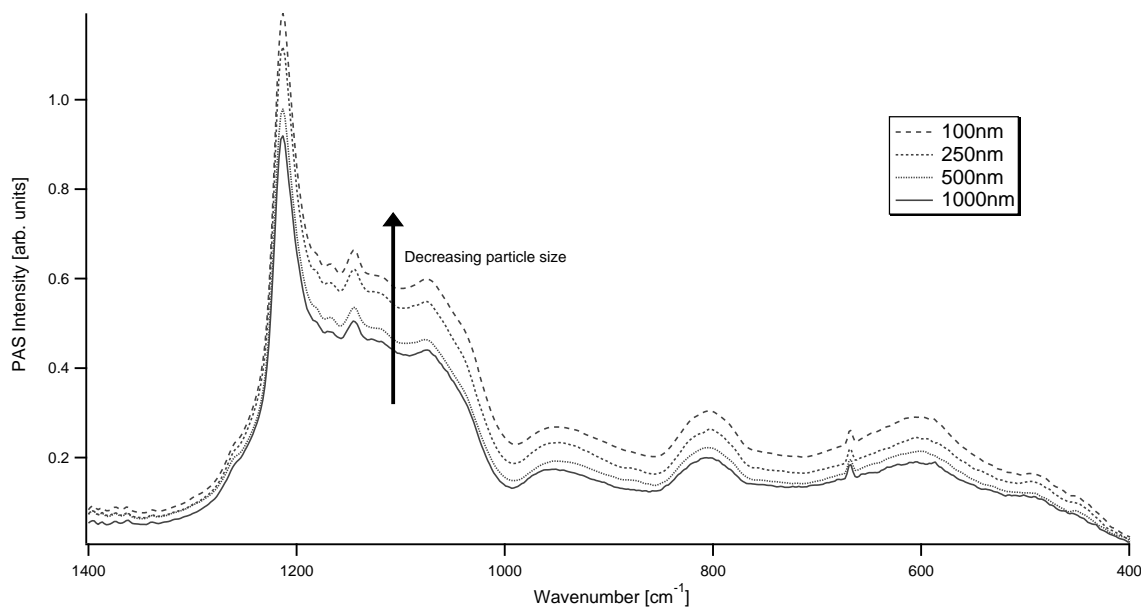


Figure 3.1: FTIR-PAS spectra of varying sized silica spheres. There is a clear increase in spectral intensity with decreasing particle size. This is attributed to the increase in surface area producing the thermal wave. Particle size appears to have no effect on peak positions, widths or relative intensities.

3.3 Results and Discussion

Figure 3.1 shows the FTIR-PAS spectrum of four different sizes of AngströmSpheres: 100 nm, 250 nm, 500 nm and 1000 nm. The signal intensity is increased for all wavenumbers as particle size decreases. As previously mentioned, this change of intensity has been linked to the increase in porosity of the samples when particle size decreases [39,43,45]. This study supports the other previous findings related to overall signal enhancement of smaller particles and extends the particle size range used to the nanometer scale.

Peak positions remain unchanged in general when detected photoacoustically. This is expected, as the peak positions are determined by the bond resonance energies, which should be unchanged for samples of the same composition such as the AngströmSpheres [1]. This is also in agreement with previous reports [43–47].

When examining the same sample in both FTIR-PAS and -Op, obvious changes to the spectrum can be observed in the drastic changes to peak shapes (see Figure 1.3). Between the two detection schemes, peak intensity increases were detected in the FTIR-PAS spectrum, as reported by others [45]. They also reported that the increase in signal is not uniform; the growth of peaks related to surface adsorbed species was found to be an order of magnitude higher than those generated by the sample. The authors offered no explanation but we suspect it is related to thermal diffusion effects; modes of surface adsorbed molecules should have the highest thermal transfer to the carrier gas. Others have suggested that modes related to surface species can be washed out with minimal levels of water vapour for FTIR-PAS studies of amorphous silica particles [49]. While this does not explain the peak intensity increase discrepancies, it may suggest why there are not more reports into this phenomena, as an experimental setup that does not account for water vapour should not be able to distinguish specific surface modes.

3.4 Connections with past FTIR-Op investigations

Until now, best practices for FTIR data collection have not been widely acknowledged for any FTIR detection scheme. This creates challenges for having confidence in identification of sample related spectral differences. Previously collected data must be re-examined, paying careful attention to the collection parameters used, if it is to be useful for quantitative analysis. In this vein, I examined past reports of size investigations using silica particles in FTIR-PAS (Sections 3.2-3.3). Considered below are experiments related to FTIR-Op and -PAS data of calcite, a crystalline form of calcium carbonate (CaCO_3).

The simple compound calcite (CaCO_3) has been shown to be an excellent study

case when examining vibrational modes [25, 26, 50]. Calcite is a crystalline material with an hexagonal planar structure in which alternating planes of calcium atoms and carbonate (CO_3^{2-}) molecules are stacked onto one another.

Previous FTIR-Op work with different calcium carbonate polymorphs showed that some of the peaks were susceptible to changes in structural ordering [23–26, 50]. In calcite certain vibrational modes show peak broadening with increasing temperature as well as with decreasing crystallinity. Samples with poor long-range ordering (more amorphous) result in an IR spectrum with broader peaks. These results suggest that FTIR-Op could be used as a screening tool for structural differences among a collection of samples. FTIR spectra will give information relating to the vibrational mode energies but they can not be used to obtain structural configurations. For this reason, it is necessary to pair with another characterization technique such as X-Ray diffraction (XRD), in which the the diffraction angles and their intensities can be used to calculate the lattice ordering.

FTIR-PAS measurements of calcite samples produced interesting results. Clearly defined, sharp peaks in the FTIR-Op measurements presented as broader, less defined features in the FTIR-PAS spectrum as has been previously observed in other samples [39, 43–45]. Low intensity peaks in FTIR-Op attributed to combination modes and isotopic variance detected *via* FTIR-PAS were significantly enhanced in much the same manor that modes of silica surface species showed significant enhancement [45]. Earlier work from the Poduska research group suggested that FTIR-PAS could be employed to study these weak peaks as they are not easily identified in FTIR-Op [25]. In his PhD thesis, Xu reported that peaks attributed to combination modes of calcite could be easily identified when the samples were examined using the PAS method [25]. The isotopic peak attributed to ^{13}C ν_2 vibration was similarly enhanced. The effect of particle size was examined by repeatedly grinding the calcite powders to produce

samples with a range of particle sizes.

At the time, it was unclear whether these interesting effects observed in calcite [25, 26, 50] and possibly silica [45] were related to the samples and the detection method. I re-examined Xu's results considering the effects of the best practice parameters that I developed. For his FTIR-PAS and -Op data, I considered the possible origin of spectral differences as a sample- or detection-related effect.

Xu used the Norton-Beer(medium) windowing function when collecting the FTIR-PAS calcite data. I have shown that the choice of different window functions have such a small effect on the output spectrum that the shift in peak intensities (relative or absolute) would not be observed above the experimental uncertainty. The data were collected using a FTIR-PAS cell that has a different geometry and uses a microphone detector. The cell does not have any reported strong resonance effects unlike the Gasera PA-301, thus the choice of mirror speed would not cause artifacts in the final spectrum [37].

Xu's calcite work showed that crystallinity differences can be extracted from the FTIR-Op spectrum [25, 50]. By examining changes to the FTIR-Op spectrum through a range of temperatures, Xu found that peaks sensitive to structural disorder are also sensitive to temperature changes in calcite samples. By fitting a single Lorentzian function, two distinct calcite peaks (ν_2 and ν_4) shifted to lower wavenumbers and decreased in intensity. The peaks positions were shown to shift to lower wavenumbers and decrease in intensity. The ν_4 peak broadened as the temperature increased, while the ν_2 remained constant within the uncertainty of the fit. The peak height also decreased more rapidly in ν_4 .

Xu's work involving FTIR-PAS detection of calcite highlighted two interesting results. He reported that:

- FTIR-PAS detection resulted in an enhancement of calcite absolute and relative

peak intensities, highlighting combination mode and isotopic related peaks that are often weak or obscured by noise in FTIR-Op detection

- FTIR-PAS relative peak intensities were independent of sample amount.

Xu suggested that the peak enhancement was related to the differences in the detection methods: FTIR-Op detects the energy absorbed by the sample whereas FTIR-PAS the amplitude the pressure wave generated in the carrier gas. The energy of the wave is proportional to the square of the amplitude. From this, Xu showed that the squares of FTIR-PAS peak intensity ratios were equal to the FTIR-Op peak intensity ratios within experimental uncertainty. With this, the link between the two different FTIR detection schemes becomes clear: it is possible that FTIR-PAS relative peak intensities could be used to assess structural ordering. My thesis work shows that Xu's results are not related to artifacts and are therefore thus linked to effects stemming from sample and detection method differences.

Theoretical studies predicting FTIR-PAS spectral features remain challenging. Modeling the photoacoustic signal generation and detection in a sample is a non-trivial task. While the peak broadening is expected to be thermal in nature and thus characterized by a Gaussian function, this is not a trivial thing to reconcile with theoretical calculations. Calculations specific to FTIR-Op detection of calcite peaks have shown that ν_4 broadens significantly more than ν_2 as crystallinity decreases. The correlation between crystallinity effects and those of temperature in calcite suggest that temperature studies could be used to identify peaks sensitive to crystallinity differences in other materials. My results validate the links made between FTIR-Op and FTIR-PAS by Xu, allowing for the use of FTIR-PAS relative peak intensity studies on the theoretical basis of past FTIR-Op research [23, 24].

3.5 Conclusions

The results of my experiments show what effects various parameters have on the FTIR-PAS spectrum and their individual importance has been discussed. Given that the outlined best practices are followed, it appears feasible that the PAS detection method could be further developed as a material structure characterization technique in much the same way that FTIR-Op has been in the past. FTIR-PAS may prove to be an invaluable tool for isotopic and combination mode analysis if we can further our understanding of whether spectral differences are correlated with structural ordering. It is my recommendation that future published results related to FTIR data (both optical and photoacoustic) include a more comprehensive listing of the experimental parameters. At minimum, this would include the phase correction method and the mirror speed along with the PAS cell used.

FTIR depth profiling experiments are unique to the PAS detection scheme. Changing the modulation frequency of the IR beam results in a change to the thermal diffusion length (the distance travelled by the thermal wave in the sample). These type of experiments are not exempt from the possibility of the spectral artifacts discussed in this thesis work and would benefit from the same recommended practices. There are more intricacies involving the mirror speed in depth profiling experiments, such that the best practices would likely need to be expanded upon. The use of homogeneous powdered silica samples in my thesis work made depth profiling experiments impractical.

The photoacoustic detection of IR vibrations is an inherently thermal process. There are obvious changes to peak shapes when comparing FTIR-Op and -PAS detection. Thermal effects are likely to play a role in this, but it is unclear how significant. This is a challenging theoretical calculation and at the time of writing I am unaware of any progress. PAS temperature experiments have been achieved using specialized

PAS cells for gas phase analysis [51] and it is possible that the idea may be extended to powders. This is a complicated experimental problem however, and beyond the scope of this thesis. Temperature studies using the PA-301 cell would be challenging. As the source of the resonance effects are not explained, it is possible that modifying the operating temperature could change the resonance response (frequency space position, intensity, etc.). An in-depth examination on the effect of operating temperature using the cantilever-based PA-301 cell (Gasera, Inc.) should be explored further in the future. It is also possible to use other commercially available photoacoustic cells, such as the microphone-based MTEC 300 used by Xu. This device has no reported resonance issues which may make it a better candidate for temperature studies. The obvious trade off is that the sensitivity of the microphone-based cell is much lower than the cantilever detector.

Chapter 4

Conclusions

4.1 Summary

The best practices developed in this thesis are relevant to both FTIR-PAS and FTIR-Op detection schemes. The guidelines outlined in Section 2.4 minimize spectral artifacts related to instrumentation, data collection and data processing procedures.

The largest artifact observed in this investigation was caused by resonance effects linked to the choice of photoacoustic cell. These effects were only relevant when high mirror speeds were used. A resonance peak is superimposed on the spectral data in frequency space. As such, the effect of the resonance is different in wavenumber space as the mirror speed shifts. Higher mirror speeds resulted in lower data acquisition time, so it is preferable to use the highest mirror speed available. For our PAS cell (PA-301, Gasera Inc.) this is up to 2.5 kHz.

The Mertz phase correction is recommended over the modulus phase correction for the reasons presented in Section 2.3.2. The Mertz method produced a higher signal in the lower wavenumber regime, which typically is preferable for our FTIR experiments. Like the windowing function, many phase correction methods have been developed

and discussed in the literature [33,36].

For our experimental setup acquisition method and windowing function had minimal impact on the final results. To decrease data collection time, I recommend forward direction acquisition. Windowing is an important part of Fourier signal processing and any of the functions included in the OPUS software, such as the: Blackman-Harris 3-Term, Norton-Beer; medium, Hamming, or Bartlett, to name a few, are acceptable.

Adjusting the co-additions results in the expected effect of improving the signal-to-noise ratio (SNR). The trade-off of high co-additions is increased data collection time. Also noted was the decrease in overall signal with increasing co-additions. This effect appeared to be uniform and thus would not affect relative peak intensities. I settled on a value that produced a high-quality spectrum in a minimal amount of time.

By applying the best practices to nanometer-scale (100 nm - 1000 nm) amorphous silica spheres, I was able to identify sample size related effects in the spectrum. Monodisperse particles of these sizes have not been examined previously. The FTIR-PAS spectrum showed an increase in overall signal intensity with decreasing particle size, as had been previously observed for larger particles and different compounds [39,45]. There were no changes to relative peak intensities, widths and positions.

As compared to FTIR-Op, the FTIR-PAS spectrum showed changes to peak shapes and intensities. Other studies have reported similar results, again with differences in sample sizes and composition [25,42,45]. Examining these previous results in the context of best practices and sample size related effects suggests that those observed changes were not due to data collection parameters or particle size effects, but in fact an effect related to the samples and/or the detection scheme.

4.2 Broader context

The necessity to undergo the parameter investigation prior to the experiments related to size effects in silica shows the need for a more standardized procedure for FTIR-PAS. While a few of the parameters were shown to have minimal impact on the results, I was not able to obtain this information during my review of the literature, forcing the execution of the experiments. Furthermore, observed differences in published spectra may still be related to more variable data acquisition and processing parameters such as the mirror speed or the phase correction, as this information seems to be rarely included in the literature. For these reasons it would benefit the community to adopt a more transparent approach when publishing and include more relevant information related to the procedures, including but not necessarily limited to those investigated in this thesis.

Particle size has been shown to have an effect on relative peak intensities in other FTIR detection schemes. My examination of monodisperse silica spheres has shown that there is not effect on relative peak intensities when using FTIR-PAS. This suggests FTIR-PAS could be used to assess structural ordering of samples using relative peak intensities, as has been done using other detection methods, but without the need to consider particle size.

The effect observed in FTIR-PAS studies of calcite [25] present an interesting avenue for future research questions. The reported relationships between relative peak intensities can be attributed to sample and detection related differences following my technical investigation of FTIR-PAS. Xu showed that relative peak intensities in FTIR-Op spectra could be used to assess structural differences between samples. His examination of FTIR-PAS presented interesting results, but until the conclusion of this thesis work it was unknown within the Poduska group whether those results could be attributed to the samples. Moving forward, further investigation should

be made into why FTIR-PAS shows peak intensity increases over FTIR-Op, specifically in the combination modes and those attributed to isotopic variations. Using the best practices I have developed in my thesis work, any progress made in that avenue can be attributed to differences between the detection schemes without fear of instrumentation and data processing artifacts.

Bibliography

- [1] R. Al-Oweini and H. El-Rassy. Synthesis and characterization by FTIR spectroscopy of silica aerogels prepared using several $\text{Si}(\text{OR})_4$ and $\text{R}'\text{Si}(\text{OR}')_3$ precursors. *Journal of Molecular Structure*, 919(1–3):140–145, doi:10.1016/j.molstruc.2008.08.025.
- [2] IGOR Pro Manual Ver. 6.0, Sep 2007.
- [3] M. P. Marder. *Condensed matter physics*. John Wiley and Sons, 2 edition, 2010.
- [4] V. R. Grandy, K. M. Poduska, and I. Saika-Voivod. Vibrational signatures of chemical- and density-induced structural changes in simulated amorphous silica. *Canadian Journal of Physics*, 92(7/8):615–618, doi:10.1139/cjp-2013-0639.
- [5] E. R. Lippincott, A. Van Valkenburg, C. E. Weir, E. N. Bunting, et al. Infrared studies on polymorphs of silicon dioxide and germanium dioxide. *Journal of Research of the National Bureau of Standards*, 61(1):61, 1958.
- [6] R. Hanna. Infrared Absorption Spectrum of Silicon Dioxide. *Journal of the American Ceramic Society*, 48(11):595–599, doi:10.1111/j.1151-2916.1965.tb14680.x.
- [7] J. Etchepare, M. Merian, and L. Smetankine. Vibrational normal modes of SiO_2 . I. α and β quartz. *The Journal of Chemical Physics*, 60(5):1873–1876, 1974.

- [8] C. J. Brinker and G. W. Scherer. *Sol-gel science: the physics and chemistry of sol-gel processing*. Academic press, 2013.
- [9] R. Salh. Defect Related Luminescence in Silicon Dioxide Network: A Review. *InTech*, doi:10.5772/22607.
- [10] N. Gopal, K. Narasimhulu, and J. Rao. EPR, optical, infrared and Raman spectral studies of Actinolite mineral. *Spectrochimica Acta Part A: Molecular and Biomolecular Spectroscopy*, 60(11):2441–2448, 2004.
- [11] A. Duran, C. Serna, V. Fornes, and J. F. Navarro. Structural considerations about SiO₂ glasses prepared by sol-gel. *Journal of Non-Crystalline Solids*, 82(1-3):69–77, 1986.
- [12] A. Bertoluzza, C. Fagnano, M. A. Morelli, V. Gottardi, and M. Guglielmi. Raman and infrared spectra on silica gel evolving toward glass. *Journal of Non-Crystalline Solids*, 48(1):117–128, 1982.
- [13] G. Bekiaris, S. Bruun, C. Peltre, S. Houot, and L. S. Jensen. FTIR–PAS: A powerful tool for characterising the chemical composition and predicting the labile C fraction of various organic waste products. *Waste Management*, 39:45 – 56, doi:10.1016/j.wasman.2015.02.029.
- [14] G. Bekiaris, J. M. Triolo, C. Peltre, L. Pedersen, L. S. Jensen, and S. Bruun. Rapid estimation of the biochemical methane potential of plant biomasses using Fourier transform mid-infrared photoacoustic spectroscopy. *Bioresource Technology*, 197:475 – 481, doi:10.1016/j.biortech.2015.08.050.
- [15] G. Bekiaris, C. Peltre, L. Jensen, and S. Bruun. Using FTIR-photoacoustic spectroscopy for phosphorus speciation analysis of biochars. *Spectrochim-*

- ica Acta - Part A: Molecular and Biomolecular Spectroscopy*, 168:29–36, doi:10.1016/j.saa.2016.05.049.
- [16] K. H. Michaelian. *Photoacoustic Infrared Spectroscopy*. Wiley-Interscience, Hoboken, N.J., 2003.
- [17] K. H. Michaelian. Invited Article: Linearization and signal recovery in photoacoustic infrared spectroscopy. *Review of Scientific Instruments*, 78(5), doi:10.1063/1.2735447.
- [18] A. Badawi, N. Al-Hosiny, S. Abdallah, S. Negm, and H. Talaat. Photoacoustic study of optical and thermal properties of CdTe quantum dots. *Journal of Materials Science and Engineering A*, 2:1–6, 2012.
- [19] A. Badawi. Photoacoustic study of alloyed Cd_{1-x}Pb_xS quantum dots sensitized solar cells electrodes. *Journal of Materials Science: Materials in Electronics*, 27(8):7899–7907, 2016.
- [20] C. Du, J. Zhou, H. Wang, X. Chen, A. Zhu, and J. Zhang. Determination of soil properties using Fourier transform mid-infrared photoacoustic spectroscopy. *Vibrational Spectroscopy*, 49(1):32–37, doi:10.1016/j.vibspec.2008.04.009.
- [21] K. H. Michaelian, B. E. Billingham, J. M. Shaw, and V. Lastovka. Far-infrared photoacoustic spectra of tetracene, pentacene, perylene and pyrene. *Vibrational Spectroscopy*, 49(1):28–31, doi:10.1016/j.vibspec.2008.04.005.
- [22] K. H. Michaelian, R. H. Hall, and K. I. Kenny. Photoacoustic infrared spectroscopy of Syncrude post-extraction oil sand. *Spectrochimica Acta Part A: Molecular and Biomolecular Spectroscopy*, 64(3):703–710, doi:10.1016/j.saa.2005.07.072.

- [23] R. Gueta, A. Natan, L. Addadi, S. Weiner, K. Refson, and L. Kronik. Local Atomic Order and Infrared Spectra of Biogenic Calcite. *Angewandte Chemie International Edition*, 46(1-2):291–294, doi:10.1002/anie.200603327.
- [24] C. Carteret, M. De La Pierre, M. Dossot, F. Pascale, A. Erba, and R. Dovesi. The vibrational spectrum of CaCO_3 aragonite: A combined experimental and quantum-mechanical investigation. *The Journal of Chemical Physics*, 138(1):014201, doi:10.1063/1.4772960.
- [25] B. Xu. *Assessing different types of disorder in carbonate minerals with vibrational spectroscopy*. PhD thesis, Memorial University of Newfoundland, St. John's, Newfoundland, October 2015.
- [26] K. M. Poduska, L. Regev, E. Boaretto, L. Addadi, S. Weiner, L. Kronik, and S. Curtarolo. Decoupling Local Disorder and Optical Effects in Infrared Spectra: Differentiating Between Calcites with Different Origins. *Advanced Materials*, 23(4):550–554, doi:10.1002/adma.201003890.
- [27] A. G. Bell. On the production and reproduction of sound by light. *American Journal of Science*, Series 3 Vol. 20(118):305–324, doi:10.2475/ajs.s3-20.118.305.
- [28] A. Rosencwaig. Photoacoustic spectroscopy of solids. *Optics Communications*, 7(4):305 – 308, doi:10.1016/0030-4018(73)90039-4.
- [29] A. Rosencwaig. Photoacoustic spectroscopy. New tool for investigation of solids. *Analytical Chemistry*, 47(6):592A–604a, doi:10.1021/ac60356a015.
- [30] A. Rosencwaig and A. Gersho. Theory of the photoacoustic effect with solids. *Journal of Applied Physics*, 47:64–69, doi:10.1063/1.322296.

- [31] F. A. McDonald and G. C. Wetsel, Jr. Generalized theory of the photoacoustic effect. *Journal of Applied Physics*, 49:2313–2322, doi:10.1063/1.325116.
- [32] K. Michaelian. personal communication.
- [33] P. R. Griffiths and J. A. de Haseth. *Fourier transform infrared spectrometry*, volume 83 of *Chemical Analysis*. Wiley, 1st edition, 1986.
- [34] The FFT in FTIR. <http://www.essentialftir.com/fftTutorial.html>. Accessed: 2017-04-19.
- [35] L. Mertz. *Transformations in optics*. Wiley, 1965.
- [36] D. B. Chase. Phase Correction in FT-IR. *Applied Spectroscopy*, 36(3):240–244, May 1982.
- [37] K. Michaelian. personal communication.
- [38] F. J. Harris. On the use of windows for harmonic analysis with the discrete Fourier transform. *Proceedings of the IEEE*, 66(1):51–83, 1978.
- [39] N. L. Rockley, M. K. Woodard, and M. G. Rockley. The Effect of Particle Size on FT-IR-PAS Spectra. *Applied Spectroscopy*, 38(3):329–334, doi:10.1366/0003702844555377.
- [40] S. Abdallah, N. Al-Hosiny, and A. Badawi. Photoacoustic study of CdS QDs for application in quantum-dot-sensitized solar cells. *Journal of Nanomaterials*, 2012:108, 2012.
- [41] R. Ruppin and R. Englman. Optical phonons of small crystals. *Reports on Progress in Physics*, 33(1):149, doi:10.1088/0034-4885/33/1/304.

- [42] P. Kristova, L. J. Hopkinson, and K. J. Rutt. The Effect of the Particle Size on the Fundamental Vibrations of the $[\text{CO}_3^{2-}]$ Anion in Calcite. *The Journal of Physical Chemistry A*, 119(20):4891–4897, doi:10.1021/acs.jpca.5b02942.
- [43] C. Q. Yang and W. G. Fateley. Proceedings of the XVIIth European Congress on Molecular Spectroscopy, The effect of particle size on peak intensities of FT—IR photoacoustic spectra. *Journal of Molecular Structure*, 141:279 – 284, doi:10.1016/0022-2860(86)80334-9.
- [44] H. Yang and J. Irudayaraj. Estimation Of Particle Size By DRIFTS and FTIR-PAS. *Particulate Science and Technology*, 17(4):269–282, doi:10.1080/02726359908906818.
- [45] M. S. Seehra and R. S. Pandurangi. Anomalous enhancement of the surface IR modes in photoacoustic spectroscopy of SiO_2 particles. *Journal of Physics: Condensed Matter*, 1(31):5301, 1989.
- [46] D. J. Schwerha, C.-S. Orr, B. T. Chen, and S. C. Soderholm. Direct-on-filter analysis of crystalline silica using photoacoustic Fourier transform-infrared spectroscopy. *Analytica Chimica Acta*, 457(2):257–264, doi:10.1016/S0003-2670(02)00023-5.
- [47] Q. Wen and K. H. Michaelian. Photoacoustic infrared spectroscopy of polymer beads. *Spectrochimica Acta Part A: Molecular and Biomolecular Spectroscopy*, 73(5):823–827, doi:10.1016/j.saa.2009.04.004.
- [48] P. S. Belton, R. H. Wilson, and A. M. Saffa. Effects of particle size on quantitative photoacoustic spectroscopy using a gas-microphone cell. *Analytical Chemistry*, 59(19):2378–2382, doi:10.1021/ac00146a013.

- [49] R. Hentschke, C. Ballnus, and J. Meyer. Remarks on the Interpretation of IR-Absorption Studies Applied to the Surfaces of Silica Nanoparticles. *The Journal of Physical Chemistry C*, 120(17):9229–9235, doi:10.1021/acs.jpcc.6b00807.
- [50] B. Xu, M. B. Toffolo, L. Regev, E. Boaretto, and K. M. Poduska. Structural differences in archaeologically relevant calcite. *Analytical Methods*, 7(21):9304–9309, doi:10.1039/C5AY01942G.
- [51] M. Niu, Q. Liu, K. Liu, Y. Yuan, and X. Gao. Temperature-dependent photoacoustic spectroscopy with a T shaped photoacoustic cell at low temperature. *Optics Communications*, 287:180 – 186, doi:10.1016/j.optcom.2012.09.023.